Front. Mater. Sci. 2023, 17(1): 230634
https://doi.org/10.1007/s11706-023-0634-z

REVIEW ARTICLE

Research and development of nanocrystalline W/W-based materials: novel preparation approaches, formation mechanisms, and unprecedented excellent properties

Zaoming Wu (✉), Qiang Li, and Xiaofeng Yang

Institute of Materials, China Academy of Engineering Physics, Mianyang 621907, China

ABSTRACT: Tungsten (W) has become the most promising plasma-facing material (PFM) in fusion reactor, and W still faces performance degradation caused by low-temperature brittleness, low recrystallization temperature, neutron irradiation effects, and plasma irradiation effects. The modification of W/W-based materials in terms of microstructure manipulation is needed, and such techniques to improve the performance of materials are the topics of hot research. Researchers have found that refining the grain can significantly improve the strength and the irradiation resistance of W/W-based materials. In this paper, novel approaches and technique routes, including the "bottom-up" powder metallurgy method and "top-down" severe plastic deformation method, are introduced to the fabrication of nanocrystalline W/W-based materials. The formation mechanisms of nanocrystalline W/W-based materials were revealed, and the nanostructure stabilization mechanisms were introduced. The mechanical properties of nanocrystalline W/W-based materials were tested, and the irradiation behaviors and performances were studied. The mechanisms of their high mechanical properties and excellent irradiation-damage resistance were illustrated. This article may provide an experimental and theoretical basis for the design and development of high-performance novel nanocrystalline W/W-based materials.

KEYWORDS: nanocrystalline tungsten; grain boundary; secondary phase doping; mechanical property; irradiation behavior

Contents

1 Introduction
2 Nanocrystalline W/W-based materials — one of the most promising plasma-facing material for nuclear fusion reactor
3 The preparation route of nanocrystalline W/W-based materials
3.1 Powder metallurgy (PM)
3.1.1 Preparation of nanocrystalline W/W-based powder
3.1.1.1 Ball milling method
3.1.1.2 Wet-chemical method
3.1.2 Powder pretreatment technology
3.1.2.1 Cold isostatic pressing molding technology
3.1.2.2 Powder tablet machine

Received July 7, 2022; accepted October 8, 2022

E-mail: wzmcaep@163.com

3.1.3 Powder sintering technology
3.1.3.1 Resistance sintering under ultra-high pressure
3.1.3.2 Hot isostatic pressing sintering
3.1.3.3 Spark plasma sintering
3.2 Severe plastic deformation (SPD)
3.2.1 High-pressure torsion
3.2.2 Surface mechanical attrition treatment
3.3 Challenges and limitations of two methods
4 The properties of nanocrystalline W/W-based materials
4.1 Vickers hardness
4.2 Irradiation behavior of nanocrystalline or nanostructured W/W-based materials
4.2.1 He ion irradiation behavior
4.2.2 Heavy ion irradiation behavior
5 Conclusions
Authors' contribution
Disclosure of potential conflict of interest
Acknowledgements
References

1 Introduction

Nuclear fusion energy is one of the most promising methods to solve the energy problem for humans. One of the keys to the realization of nuclear fusion energy is to solve the problem of materials, especially plasma-facing materials (PFMs). The service environment of PFMs in nuclear fusion reactors is very harsh. Therefore, the safe service of PFMs is very important and determines the operating state of nuclear fusion reactors. The components that directly contact plasma in nuclear fusion reactors include the first wall, divertor, and limiter [1–4]. The service environment of PFMs includes high-temperature edge plasma (about 1000 °C), steady-state high heat flow (first wall: 1 $MW \cdot m^{-2}$, divertor: 10 $MW \cdot m^{-2}$), and transient thermal shock ($GW \cdot m^{-2}$). The high temperature and high heat flux service environment will recrystallize, crack, and melt the surface of PFMs. High-energy (14.1 MeV) neutron irradiation, low-energy (first wall: 100 eV, divertor: several eV) high-flux (first wall: 10^{20}–10^{21} $m^{-2} \cdot s^{-1}$, divertor: 10^{25} $m^{-2} \cdot s^{-1}$) D (deuterium)/T (tritium) + 5% He (helium) plasma irradiation, and other particle streams of coordinated irradiation can cause damage to materials (vacancies, interstitial atoms, dislocation, etc.), a hydrogen helium effect (hydrogen helium bubble, swelling, embrittlement, etc.), and a neutron radiation transmutation effect (composition change, activation, etc.) [5–13].

It is necessary to focus on the interaction between PFMs and the particles, and the influence of the service environment on the performance of PFMs. In the fusion reactor, uncharged high-energy particles include neutrons, photons, and other particles that are not constrained by the magnetic field, and these particles directly act on the first wall and cause sputtering, spalling, off-site damage, etc., of material surface. Charged particles escape from the plasma edge, due to the incomplete plasma confinement, and interact with the first wall material. These particles are mainly low-energy deuterium, tritium, and a small amount of helium plasma, and these particles can cause the etching, gas-bubble, and fuzz-like nanostructure formation of materials. Furthermore, since the first wall is used as a heat transfer device, the thermal conductivity of the material is required to be good enough for higher heat transfer efficiency and energy output yield. Therefore, a low sputtering yield, high thermal conductivity, high melting point, and good plasma compatibility of PFMs are required in order to make the nuclear fusion reactor device operate in a stable state, and to realize the safe and reasonable utilization of nuclear fusion energy [7].

Tungsten (W) possesses a high melting point (3410 °C), low thermal expansion coefficient (4.5×10^{-6} K^{-1} at 25 °C), good thermal conductivity (173 $W \cdot m^{-1} \cdot K^{-1}$ at 25 °C), low sputtering corrosion rate, low H retention, and excellent high-temperature strength [2,6,8–9]. W is confirmed to be the only candidate for plasma-facing materials in the International Thermonuclear Experimental Reactor (ITER) by experts and scholars. W has received increasing attention as PFMs, and the good compatibility of W materials with plasma has been confirmed. Therefore, W materials have become the most likely PFMs to adapt to fusion reactors [14–16].

2 Nanocrystalline W/W-based materials — one of the most promising plasma-facing material for nuclear fusion reactor

As PFMs, W materials still face performance degradation caused by low-temperature brittleness, low recrystallization temperature, neutron irradiation effects, and plasma irradiation effects [5–13].

Low-temperature brittleness: The ductile-to-brittle transition temperature (DBTT) of pure W is about 400 °C,

showing low-temperature brittleness [6]. The yield strength (σ_s) and fracture strength (σ_f) of tungsten materials decrease with the increase of temperature, and the crossing point of "yield strength and fracture strength versus temperature" curves is DBTT. The factors affecting the DBTT of tungsten materials include: metal alloy element composition, grain size, defects in materials and effect of heat treatment [17]. W materials in fusion reactor face high temperature and low energy high flux D/T + 5% He plasma irradiation, and these multiple particle streams plasma irradiation can cause off-site damage to materials, such as vacancies, interstitial atoms, and dislocations [10]. Hydrogen retention in materials could lead to bubbles, swelling, embrittlement, cracking of W materials, and these irradiation effects will lead the brittleness and the decrease of ductility of W materials [10–13,18–19]. It is necessary to decrease the DBTT of W materials and improve the low-temperature brittleness of W materials.

Low recrystallization temperature (RCT): The recrystallization temperature range of W is 1150–1350 °C, which is too low. When the temperature is higher than the recrystallization temperature, the size of the grains of W will grow up, as shown in Fig. 1 [7]. The mechanical properties, such as the yield strength and hardness of the material, decrease with the increase of the grain size, according to the Hall–Petch formula. In a nuclear fusion reactor, the transient temperature of the environment generally exceeds the recrystallization temperature of pure W. Plasma-facing W materials operate at a steady-state temperature between DBTT and RCT, as shown in Fig. 1 [7]. When the temperature is lower than DBTT, the material exhibits low-temperature brittleness, making the W material more easily prone to fracturing. When the temperature is higher than RCT, the W grain size will increase significantly, which will reduce the strength and other properties of the material. To better use W materials in fusion reactors, a method must be found to increase the recrystallization temperature of W materials.

Neutron irradiation effect: In fusion reactors, the fusion reaction is mainly deuterium tritium fusion reaction, i.e., T + D → He + n + 17.6 MeV. The reaction releases 17.6 MeV energy, of which the energy of the neutron is about 14.1 MeV (which can be calculated according to the conservation of momentum), and the energy of neutron is particularly high. After plasma-facing materials are irradiated by high-energy neutrons, the materials will produce off-site damage, including defects such as

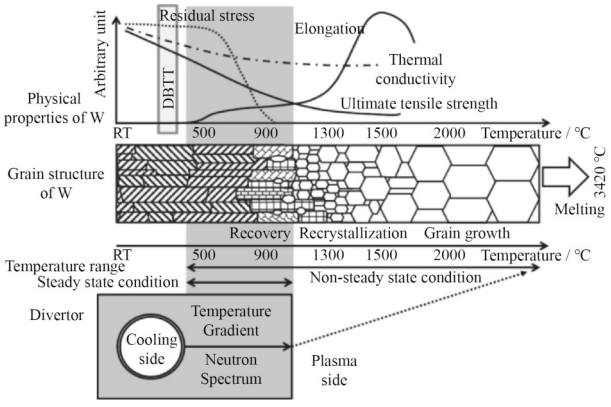

Fig. 1 The variation of the W grain size and material properties with temperature. Reproduced with permission from Ref. [7].

vacancies, interstitial atoms, and dislocations. Meanwhile, the neutron irradiation effect causes the material to undergo nuclear transmutation, resulting in a series of transmutation products, such as helium and hydrogen, causing the material swelling. Therefore, it is necessary to find a way to improve the irradiation resistance of the material [8–9].

Plasma irradiation effects cause degradation of material properties, such as swelling, cracking, blistering, and fuzzing of materials. The ion implantation leads to pre-irradiation damage, and the atoms leave their original positions to form self-interstitials, and, at the same time, the original positions that the atoms leave form vacancies. Furthermore, the ion irradiation leads to the sputtering of W atoms, and craters are formed by the etching of implantation atoms on the W's surface. The implantation atom forms an impurity-interstitial atoms in the W materials. Dislocation lines can be formed through the aggregation of defects. The self-interstitials form interstitial loop. The vacancies gather together and form void. The implantation gas atoms can form bubble and blistering at the interior and surface of W. The vacancy and self-interstitial atoms create an Frenkel pair annihilation effect and disappear. The self-interstitial atoms and impurity-interstitial atoms migrate and form a mixed cluster [10]. The W atom also undergoes nuclear transmutation and becomes a Re atom. The plasma irradiation effect will cause cracking, swelling, blistering, and fuzzing on the surface of the pure W material, as shown in Fig. 2 [11–13]. The irradiation effect will lead to the sputtering, etching, etc. of PFMs, and a large number of impurity particles are generated. The impurity particles enter into plasma, and pollute the plasma in the core of the

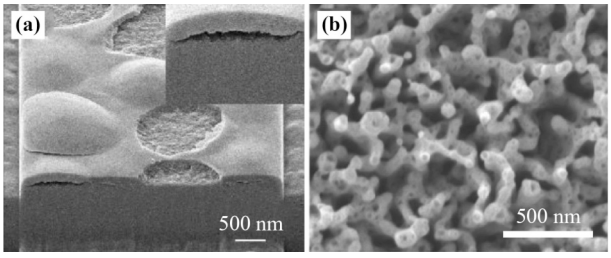

Fig. 2 Plasma irradiation causes (**a**) the swelling, cracking, and blistering behavior on the surface of pure W material, and (**b**) the fuzz behavior. Reproduced with permission from Refs. [11–12].

fusion reactor, which leads the degradation of plasma quality, and affects the stability and service life of the nuclear fusion reactor.

W and W-based materials have salient features to be used as PFMs. However, they suffer from many problems, as mentioned above. Their modification in terms of microstructure manipulation is needed, and such techniques to improve the performance of materials are the topics of hot research. Researchers have found that refining the grain can significantly improve the strength [20–22] and the irradiation resistance [23–25] of the material. Refining W grains can increase the volume fraction of grain boundaries (GBs). The nanocrystalline material can be regarded as the material composed of two "phases" of grains and GBs. The GBs act as barriers, hindering the movement of dislocations, thereby increasing the strength of the material (such as hardness and yield strength). Grain refinement can reduce the DBTT of the material and improve the low-temperature brittleness of W materials. At the same time, the GB can absorb defects generated by irradiation, thereby significantly improving the irradiation resistance of the material. The second phase particle dispersion is another way to improve the properties of W-based alloys by suppressing the growth of W grains and dispersion strengthening. Therefore, nanocrystalline W-based materials may improve some properties of pure W materials.

Nanocrystalline W alloy with dispersed particles is one of the most promising methods to overcome the application limitations of pure W. It is difficult to keep the W grains at the nanometer level and obtain a high density at the same time, due to the contradiction between the low recrystallization temperature (1150–1350 °C) and high melting point (3410 °C) of pure W. The W grains in the nanocrystalline powder are in a metastable state, and the temperature at which the grains grow is lower than 1000 °C, so it is particularly difficult to prepare nanocrystalline W and W alloys with a high density, uniform microstructure, and composition.

This article will introduce innovative methods for preparing nanocrystalline W/W-based alloys, including powder metallurgy, severe plastic deformation, and the selection and doping of secondary phase particles. This article also clarifies the preparation mechanism of nanocrystalline W/W-based alloys and provides theoretical basis and experimental data support for the subsequent optimization of process parameters and controllable preparation of nanocrystalline W/W-based alloys. This article introduces the mechanical properties and irradiation behavior of nanocrystalline W/W-based alloys, revealing the influence and mechanism of material microstructure, second-phase particle selection, and doping mode of secondary-phase particles on material properties.

This article introduces the nanostructure stabilization mechanism of nanocrystalline W/W-based alloy materials, the physical mechanism of particle–material interaction, and the physical mechanism of material irradiation damage, in order to design and develop a high-performance nanocrystalline W/W-based alloy with excellent mechanical properties and high irradiation resistance. This article may provide an experimental and theoretical basis for the problems faced by plasma-facing W/W-based alloys.

3 The preparation route of nanocrystalline W/W-based materials

According to the foregoing, the current problems of pure W materials mainly include a high ductile–brittle transition temperature (low temperature brittleness), low recrystallization temperature, and irradiation degradation. Refining the grain size of W can improve the properties. At present, there are two main methods for the preparation of nanocrystalline W and W-based materials: the "bottom-up" powder metallurgy method and the "top-down" severe plastic deformation method [26–27]. Figure 3 shows the preparation routes of nanocrystalline W/W-based materials, and the technical roadmaps of two main methods "bottom-up" and "top-down" are presented; and another method, magnetron deposition, was also introduced to prepare nanostructured W film.

Powder metallurgy uses metal/metal powder (or

metal/non-metal powder) obtained by mechanical alloying (MA), wet chemical methods, and other methods as raw materials, and then shape and sinter them to finally prepare metal bulk materials and composite bulk materials. Powder metallurgy usually includes the preparation of powder precursors and the sintering of powder precursors to prepare bulk materials. Common methods for preparing powder precursors include MA methods [28–30] and wet chemical methods [31–33]. MA is a process in which the starting materials, such as metal/metal powders or metal/non-metal powders, are subjected to high-energy ball milling. High-energy grinding balls impart very kinetic energy to powders to facilitate the nano-grains or alloyed powder formation through the long-term violent impacts and collisions between the powder particles and the grinding balls. Different powder particles are mixed uniformly by causing the powder to weld and break. The preparation technology, from small-scale ball mills for laboratory use to large-scale ball mills for industrial applications, can meet the dosage requirements of powder precursors for scientific research and industrial production. The other method used to prepare powder precursors is the wet chemical method. The sol-gel method is a typical representative of the wet chemical method. Nanoparticles with a core–shell structure can be prepared by using the sol-gel method. The secondary phase particles or the nitrates of metal elements are hydrothermally treated in a certain pH solution environment and then reduced with hydrogen to form core–shell structure nanoparticles with the secondary phase particles within W particles. This method is mature in technology and can be used to prepare core–shell-structure W-coated nanoparticles in large quantities, and it meets the requirements of industrial applications.

In powder metallurgy, the method of sintering the powder precursor into bulk materials generally includes hot isostatic pressing (HIP) sintering [34–35], resistance sintering under ultra-high pressure (RSUHP) [36–37], spark plasma sintering (SPS) [38–43], microwave sintering (MWS) [44–46], etc.

The severe plastic deformation method is a processing method that directly refines the crystal grains of the bulk material and uses a large amount of shear strain to refine the crystal grains of the bulk material. The bulk material obtained by this method is dense, and this method has great advantages for the preparation of ultrafine-grained and nanocrystalline materials. Severe plastic deformation methods generally include equal channel angular extrusion (ECAE) [47–49], high-pressure torsion (HPT) [48,50–51], surface mechanical attrition treatment (SMAT) [52–54], accumulative roll bonding (ARB) [55–56], etc. The schematic diagrams of these methods are shown in Fig. 4. The abovementioned common severe plastic deformation methods are widely used in the industrial field. At present, they have shown good

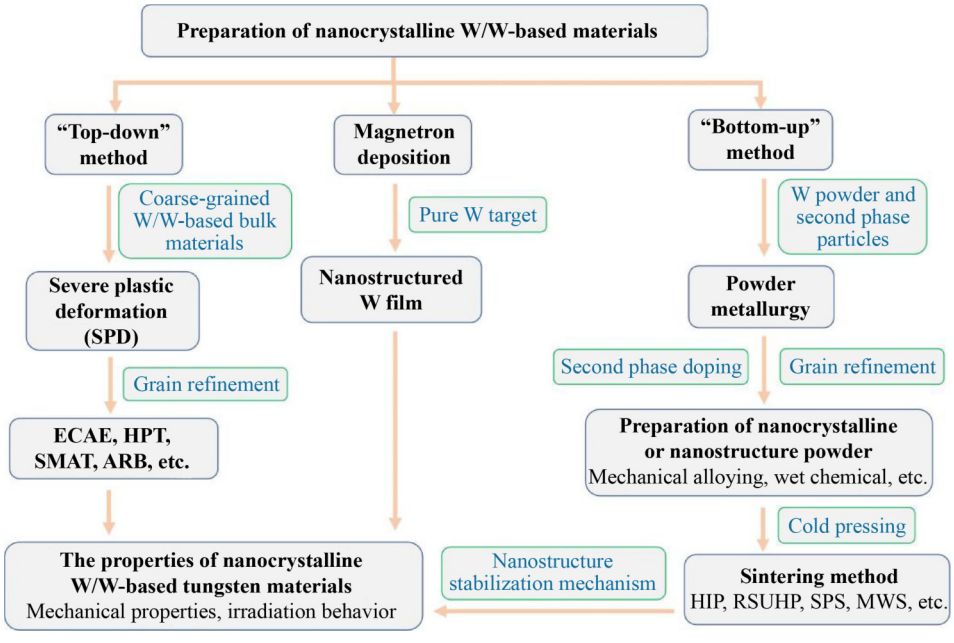

Fig. 3 The preparation routes of nanocrystalline W/W-based materials.

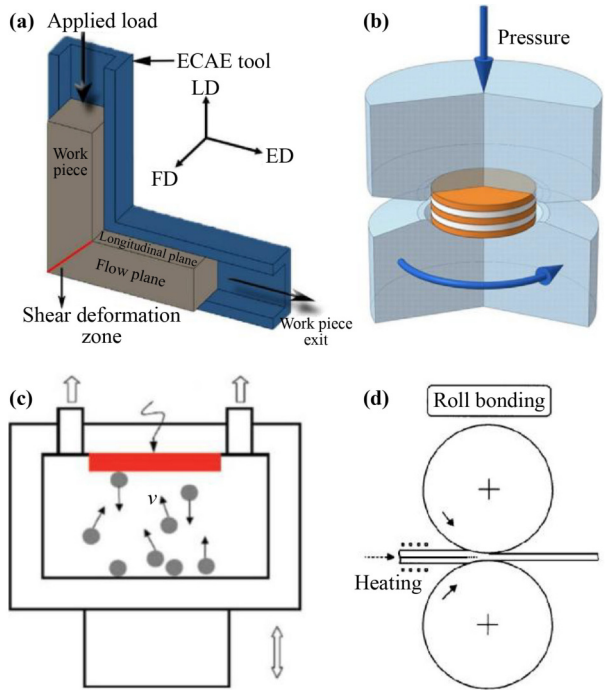

Fig. 4 The principle diagram of severe plastic deformation methods: (**a**) equal channel angular extrusion (reproduced with permission from Ref. [49]); (**b**) high-pressure torsion (reproduced with permission from Ref. [51]); (**c**) surface mechanical attrition treatment (reproduced with permission from Ref. [54]); (**d**) accumulative roll bonding (reproduced with permission from Ref. [55]).

application prospects in the field of preparing ultrafine-grained W materials. Severe plastic deformation methods cause the material to produce relatively more defects due to the dislocation of the lattice atoms in the material, so, generally the bulk materials obtained by severe plastic deformation methods need to be annealed at a certain temperature to eliminate the defects in the material. At present, the powder metallurgy method and the severe plastic deformation method can be used together to make the grain size and density of the material meet the demand.

At present, there are two ways to improve the properties of W materials: The first includes the optimization of sintering parameters, hot-pressing plastic deformation, rolling, etc.; The second includes changing the compositions of W-based materials by the secondary-phase doping. The performance of W materials can be improved through dispersion strengthening, solid solution strengthening, alloy strengthening, and other methods. According to the type of doped secondary-phase particles, W-based materials are generally divided into carbide-reinforced W-based composite materials (such as TiC, ZrC, and TaC) [57–61], oxide-reinforced W-based composite materials (such as Y_2O_3 and La_2O_3) [62–64], metal-reinforced W-based materials (such as Cr, Y, Ti, Ni, Fe, K, Cu, and Sc), and fiber-reinforced W-based composite materials (such as W fibers and carbon fibers) [65–66]. The second phase particles alloying can improve the properties of materials, such as mechanical properties, thermal properties, irradiation resistance, oxidation resistance, and corrosion resistance [67–70]. Carbides can inhibit the grain growth of W, and some carbides can form a coherent structure with W. Oxides can also inhibit the grain growth of W through pinning effect. Some metal elements can form a stable nanocrystalline structure with W through the reduction of Gibbs free energy. Figure 5 shows a stability diagram of the nanostructure of W-based materials at 1100 °C [71]. For example, the addition of certain elements such as Cr, Ti, and Sc can reduce the Gibbs free energy of the system. By characterizing and analyzing the grain size of Ti-doped and Ti-undoped ball-milled W powder annealed at 1100 °C for one week, it is found that adding the Ti element of the second-phase metal to W can effectively suppress the growth of W grains. W forms a stable nanocrystalline structure with the Ti element, as shown in Fig. 6 [71]. The adding of fibers can improve the thermal conductivity, for example, carbon fibers, and it can also increase the toughness and hardness of the materials. Surface coating techniques is also another method to improve the properties of materials

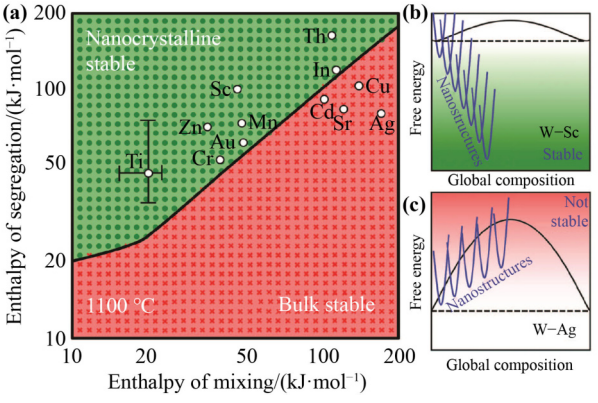

Fig. 5 Stability diagram of nanostructure of W-based materials at 1100 °C. (**a**) Diagram of nanocrystalline stable structure and nanocrystalline unstable structure: based on the mixing enthalpy and segregation enthalpy of the two elements, the Gibbs free energy value of the material is calculated and determined. (**b**) W–Sc nanocrystalline stable structure: the addition of Sc leads to a decrease in Gibbs free energy. (**c**) W–Ag nanocrystalline unstable structure: the addition of Ag leads to an increase in Gibbs free energy. Reproduced with permission from Ref. [71].

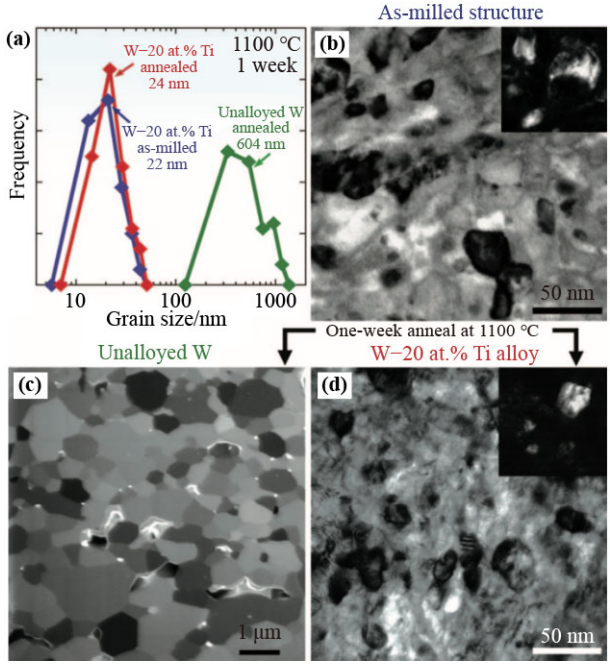

Fig. 6 Ti-doped and Ti-undoped ball-milled W powder after annealing at 1100 °C for one week. (**a**) The grain size statistics before and after annealing: (i) W without mechanical alloying; the average grain size after annealing is 604 nm; (ii) mechanical W–20 at.% Ti alloy with the average grain size of 22 nm, and the average grain size after annealing is 24 nm. (**b**) TEM image of W–20 at.% Ti after mechanical alloying (the average grain size is 22 nm). (**c**) SEM image of W without mechanical alloying after annealing (the average grain size of 604 nm). (**d**) TEM image of W–20 at.% Ti after mechanical alloying and annealing (the average grain size is 24 nm). Reproduced with permission from Ref. [71].

[72–74], such as improving oxidation resistance to avoid volatilization and disintegration of tungsten alloy when nuclear reactor cooling accident happens.

At present, secondary-phase particle doping can improve some properties of the W material, and some of the properties will be reduced. The actual engineering application needs to consider the comprehensive properties of the material. The selection of the second phase and the ratio of the second phase addition, as well as the preparation method of the powder precursor and the selection of sintering conditions, are very important to improve the overall performance of the material.

In summary, the preparation method of nanocrystalline W alloy includes the preparation of nanocrystalline powder precursors, the doping of secondary phase particles to inhibit the growth of W grains, the sintering of powder precursors, and the subsequent severe plastic deformation of bulk material.

3.1 Powder metallurgy (PM)

3.1.1 Preparation of nanocrystalline W/W-based powder

3.1.1.1 Ball milling method

The first step in the preparation of nanocrystalline W alloy is to obtain nanocrystalline W powder, and W grains can be refined by ball milling. Common types of ball mills include vibrating ball mills, rolling ball mills, planetary ball mills, and stirring ball mills.

Nanocrystalline W powder can be obtained by high-energy planetary ball mills. The high-energy ball-milling method can be divided into dry milling and wet milling according to whether process control agents (PCAs) are added. Dry milling means that only grinding balls and W powder are added to the ball-milling vessel. In wet grinding, in addition to the grinding balls and W powder, the PCA is also added, and the common PCA includes ethanol, acetone, stearic acid, etc. The addition of an appropriate amount of process control agent can improve the grinding efficiency.

Oda et al. revealed the mechanism of nanograin formation in W and obtained the nanocrystalline W powder by high-energy dry milling [30]. Coarse-grained W powder was ball milled for 100 h, and the ball-milled powder at different milling time was sampled. Oda et al. concluded that the grain refinement in W through transmission electron microscopy (TEM) microstructure characterization (at different milling time) was as follows: In the first stage, the W grain is divided by dislocations and forms into many sub-grains; In the second stage, the nanolayer structures are formed after W sub-grains are deformed by the milling balls; In the third stage, the nanolayer structure is divided into two or more nano sub-grains; In the final stage, nano sub-grains rotate to become nanograins with high-angle GB, which means that a nanolayer subdivision forms the nanograin structure.

In the dry-milling process, W powder is subjected to severe plastic deformation, and cold welding occurs between the W particles. This would impede the further fracturing of W powder, and the addition of PCA could minimize cold welding and caking through the adherence of the powder's surfaces. Every single W particle can be impacted uniformly due to the addition of PCA, as it can act as a surface-active agent, and the efficiency of high-energy ball milling can be improved. The energy (E) required for the physical process of size reduction is given

by $E = \gamma \times \Delta A$, where γ refers to the specific surface energy, and ΔA is the increase of the surface area in the milling process. The addition of PCA can reduce E, as the PCA adheres to the surface of W powder. The surface tension of ball-milled W can be reduced by the addition of PCA, and the milling time required to refine the W powder is reduced.

The cold welding and caking phenomenon of milled powder were decreased during the wet-milling process, and nanoscale powder with a uniform particle size was obtained. Wu et al. [75] conducted the experiment of wet milling on coarse-grained W powder and explored the changes of particle size and grain size during the high-energy ball-milling process. The refinement process and mechanism of W powder were studied through the analysis of microstructure and morphology of milled W powder at different milling periods. Figure 7(a) shows the morphology of the initial W powder, and it possesses polyhedral morphology with micron-scale particle size. The impact and the shear forces of milling balls act on W powder particles at the early stage of ball milling, and the W powder particles are compressed and deformed. At the same time, two or more W powder particles are welded together to form a larger particle.

The welding of W powder appears under the impact of milling balls, as shown in Fig. 7(b). The particles become flake structures with an average particle size of 460 nm due to the continuous impact and accumulation of deformation. The flake structure of W powder gets thinner and larger with the increase of milling time, as shown in Figs. 7(b) and 7(c), and the average particle size of the W powder after 20 h increases to 2.0 μm. The thickness of W powder decreases, and the size of W particles increases in the two-dimensional direction. Microcracks appeared when the flake W powder become very thin, and the W powder gradually smashed. The nanoparticles fell off from the flake W powder after being ball milled for 40 h, as shown in Fig. 7(d), and the W powder was further refined, as shown in Fig. 7(e). Finally, nanosized W particles were obtained due to the pulverization of flake W particles, as shown in Fig. 7(f).

Figure 8 shows bright-field and dark-field TEM images of W powder after being ball milled for 60 h, respectively [75]. Many nanoscale grains marked by yellow arrows appear in W particles. The selected area diffraction spots in Fig. 8(a) form the circle, which demonstrates the formation of nanocrystalline W, and Fig. 8(b) shows the nanograin of W powder, with a grain size of 5–15 nm marked by yellow arrows.

3.1.1.2 Wet-chemical method

The wet-chemical method is one of the most promising methods to prepare core–shell nanostructured powder, such as TiC/W and La_2O_3/W core–shell nanostructured powder. Carbides and oxides are distributed inside the W particles [31–33,76]. The wet-chemical process has been demonstrated to be effective in fabricating complex nanostructured materials with a very high purity and homogeneity. Yan et al. prepared core–shell nanostructured

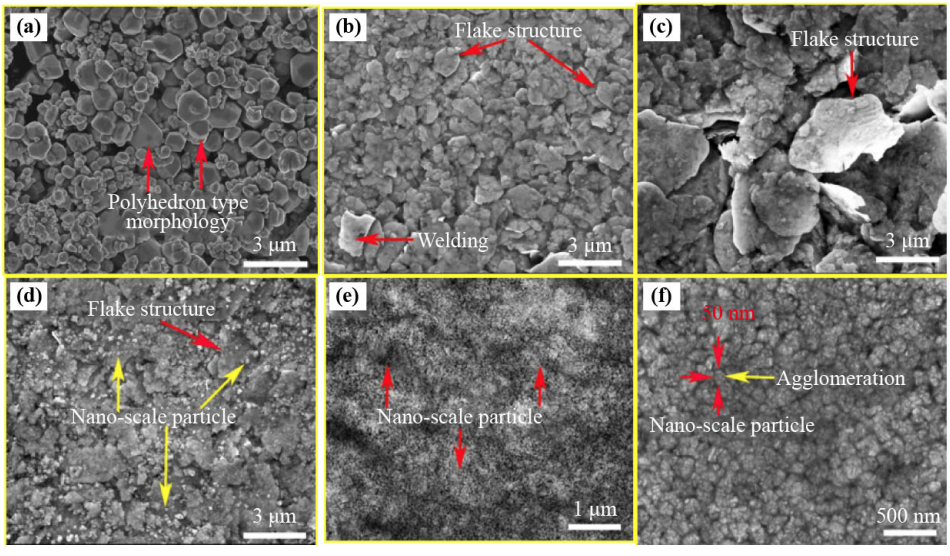

Fig. 7 SEM images of W powder ball-milled at different milling time: (**a**) 0 h; (**b**) 10 h; (**c**) 20 h; (**d**) 40 h; (**e**) 50 h; (**f**) 60 h. Reproduced with permission from Ref. [75].

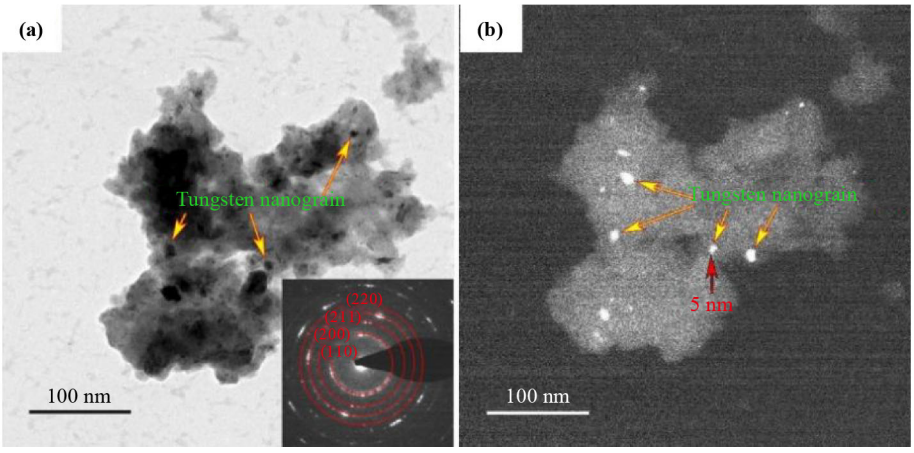

Fig. 8 TEM images of W particles ball-milled for 60 h: (**a**) bright-field image; (**b**) dark-field image. Reproduced with permission from Ref. [75].

TiC/W with a particle size of 50–200 nm [32]. A total of 3 g of AMT ($(NH_4)_6H_2W_{12}O_{40}$) powder was dissolved in de-ionized water, with stirring continuously, to form an apparent solution, and then the hydrochloric acid was added dropwise into the above solution until the desired pH of the solution was obtained. The ultrasonic dispersed TiC powders were added into the obtained solution. The as-prepared mixture solution was stirred persistently at 700 °C until the powders were precipitated. The as-prepared powders were processed by washing, filtering, drying, and reduction successively. The SEM images of TiC/W core–shell nanoparticles prepared by one-step reduction at 800 °C for 1 h are shown in Fig. 9 [32].

Yan et al. also prepared core–shell nanostructured La_2O_3/W with a particle size of 50–200 nm. Figure 10 shows the SEM image of W particles (with La_2O_3 core) [31], and they possess uniform diameters of about 50 nm. The hydrothermal-hydrogen reduction method and co-precipitation method were proposed to prepare W−La_2O_3 core–shell structure nanoparticles [31,33].

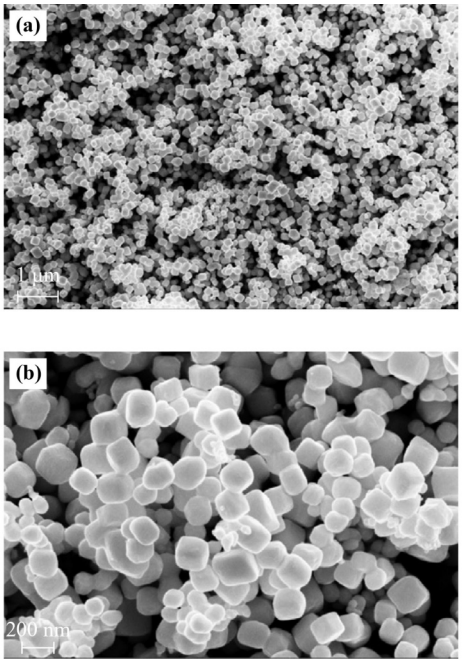

Fig. 9 SEM images of TiC/W core–shell nanoparticles prepared by one-step reduction at 800 °C for 1 h: (**a**) at low-magnification; (**b**) at high-magnification. Reproduced with permission from Ref. [32].

3.1.2 Powder pretreatment technology

Powder pretreatment generally refers to compacting and degassing the powder to prepare powder compact precursor for the subsequent sintering process. If hot isostatic pressing (HIP) sintering is used to prepare bulk materials, the powder needs to be press-formed first, and the press-formed compact is encapsulated with stainless steel, and then the press-formed compact is degassed. Hot isostatic pressing sintering is performed on the press-formed and degassed compact to obtain bulk materials. The powder also needs to be pressed before RSUHP, so that the powder has a certain strength and shape, and it is convenient to assemble the powder compact into the mold. Common powder pretreatment technologies in laboratories include cold isostatic pressing molding technology and powder tablet press molding technology.

3.1.2.1 Cold isostatic pressing molding technology

Cold isostatic pressing molding technology is a molding technology that presses powder into a certain density and

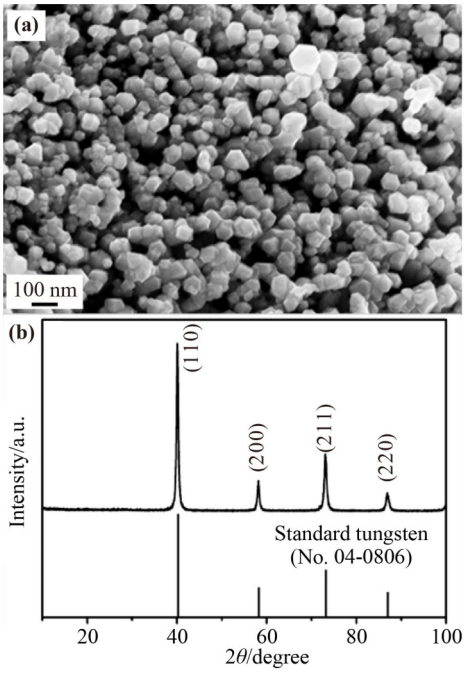

Fig. 10 (**a**) SEM image of the one-step reduced W (with La_2O_3 core). (**b**) XRD pattern showing the purity of the W (with La_2O_3 core). Reproduced with permission from Ref. [31].

a certain shape. Its compositions include elastic molds, ultrahigh-pressure vessels, hydraulic systems, and auxiliary equipment. The powder samples are pressed uniformly from all directions by using the incompressible nature of the liquid medium and the property of uniform pressure transmission. The technique of forming a compact body by the abovementioned method is called the cold isostatic pressing technique. Powder compacts with certain density and shape are required before hot isostatic pressing sintering and pressureless sintering.

3.1.2.2 Powder tablet machine

The powder tablet press is widely used in powder metallurgy, pharmacy, electronic components, and other fields. It is one of the necessary pieces of equipment for pressing granular powder into flakes with a certain strength. Molds of different specifications and sizes can be customized according to requirements, and the material of the molds can be determined according to the hardness of powder material. Common tools include tool steel, cemented carbide molds, etc. W powder has a relatively high hardness, and cemented carbide molds are generally used. The specific steps are as follows: after loading the powder into the mold, pressure is applied to the powder to make the powder have a certain shape and strength through the powder tablet press, and then the materials are demolded to obtain a cylindrical compact. The diameter of the compact is determined by the inner diameter of the customized mold, and the height is determined by adding with different volumes of powder according to the needs. The maximum pressure applied is determined by the maximum pressure that the powder tablet machine can provide and the diameter of the powder to be pressed. The pretreatment of the powder not only can obtain the powder compact which can be easily put into the sintering mold, but also can improve the density of the sintered bulk material.

3.1.3 Powder sintering technology

3.1.3.1 Resistance sintering under ultra-high pressure

RSUHP is a method of heating the powder precursor by energizing the Joule heat. This method presses the powder precursor into a powder compact with a hydraulic press to achieve a certain density, and then places the powder compact into the sintering mold for ultrahigh-voltage energization sintering. The sintering mold is generally cube-shaped and made of pyrophyllite. The cube is hollowed out to form a cylinder, which is used to fill discs or cylindrical powder compacts. The surroundings are filled with boron nitride, graphite flakes, molybdenum flakes, ring-shaped graphite heater, conductive steel ring, aluminum foil, etc. The schematic diagram of powder loading is shown in Fig. 11. The powder is compressed by six indenters, and the sintering mold of the embryo is pressurized. The pressure can reach the GPa level, and this pressure is much higher than the pressure provided by the currently known sintering method. The powder is heated by the Joule heat to achieve the densification of the powder embryo. This method is characterized by an extremely high sintering pressure, while the sintering time can range from a few minutes to several hours, and the sintering temperature is controllable. It is suitable for the sintering of ceramics, refractory metals, synthetic diamonds, and other materials, and it is especially suitable for ultrafine-grained and nanocrystalline W materials.

For the preparation of nanocrystalline W-based materials, it is necessary to overcome the contradiction between the high melting point and low recrystallization temperature of the material to obtain high-density nanocrystalline W-based materials. When the sintering

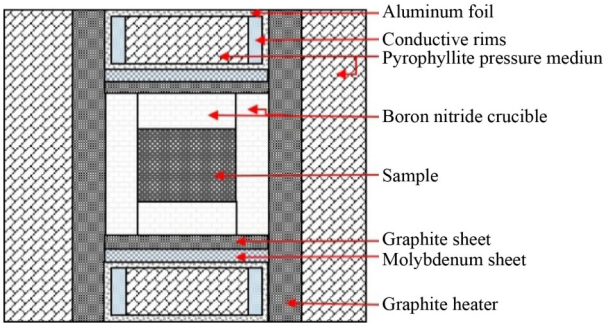

Fig. 11 Schematic diagram of powder loading during RSUHP.

temperature is low, the sintering process needs to be adjusted, and ultra-high pressure should be applied to the sintered compact to increase the density of the sintered material. Wu et al. successfully prepared W–5 wt.% Y_2O_3 (WYO) material with an average grain size of 10 nm through the second phase doping and high-energy ball milling combined with ultrahigh-pressure low-temperature sintering technology, and the density of WYO is 94.1%. The sintering temperature is 1000 °C, and the sintering pressure is 6 GPa with the sintering time of 3 h. The TEM image and grain-size statistics of the sintered material are shown in Fig. 12 [77].

Figure 13 shows TEM and high-resolution transmission electron microscopy (HRTEM) images of the sintered WYO [77]. The TEM image in Fig. 13(a) shows different nanocrystalline grains, and the corresponding fast Fourier-transform (FFT) diffraction pattern at the bottom right side confirms the existence of the nanocrystalline structure. Figure 13(b) is an HRTEM image showing W and Y_2O_3 nanoparticles. Y_2O_3 grains are distributed among W (1 1 0) crystal grains. The corresponding FFT diffraction image at the bottom right also confirms the presence of the nanocrystalline structure. Large-angle GB with an orientation angle difference of 18.1° was found between the two W crystal grains. The doping mode of Y_2O_3 is intergranular doping, and it prevents GB sliding through pinning and inhibits the grain growth of W.

Wu et al. used the RSUHP method to prepare nanocrystalline W alloy with a sintering temperature lower than RCT and successfully prepared a nanocrystalline W–5 wt.% Y_2O_3 (WYO) alloy with an average grain size of 10 nm for the first time in the world.

3.1.3.2 Hot isostatic pressing sintering

Hot isostatic pressing (HIP) sintering is a processing and molding technology that uses high-temperature and high-pressure gas that is balanced in all directions to obtain bulk materials, and this sintering method can achieve densification sintering of powder compact or pre-sintered bodies. The products obtained by this method have good uniformity and a high density.

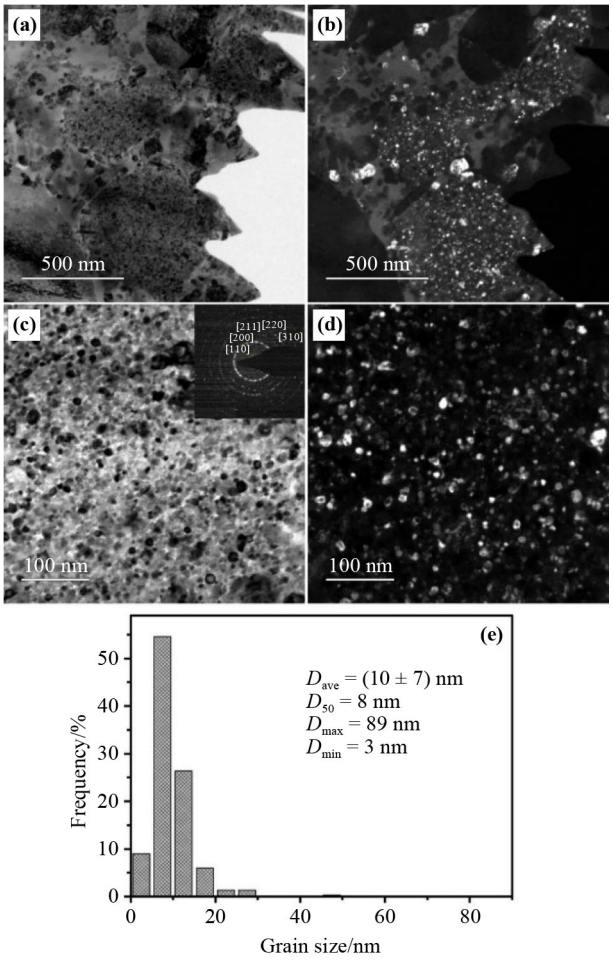

Fig. 12 (**a**)(**c**) Bright-field TEM images of sintered WYO, (**b**)(**d**) dark-field TEM images of corresponding areas, and (**e**) statistical distribution of the grain size. Reproduced with permission from Ref. [77].

The hot isostatic pressing sintering needs to encapsulate the obtained powder precursor first, and then it needs to be put it into the chamber to fill with nitrogen or inert gas to make the pressure reach a certain level, and the current pressure can reach about 200 MPa. The heat and pressure preservation are carried out when the setting sintering temperature and pressure are reached. Generally, the powder will be deformed greatly under uniform high pressure, so that the powder can be densified and sintered. This method is particularly suitable for the processing and shaping of large workpiece materials and the welding of two or more materials. At present, the hot isostatic

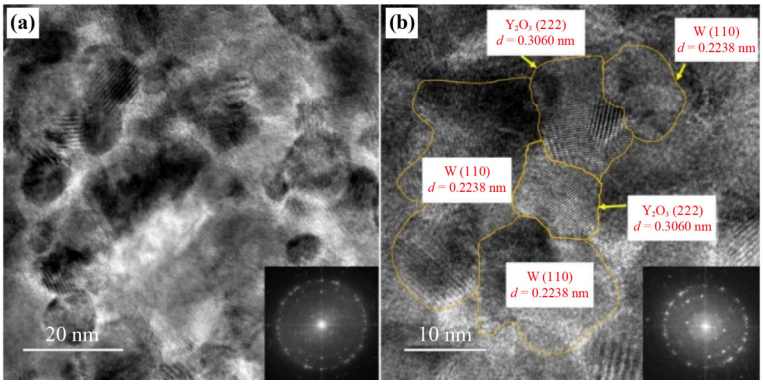

Fig. 13 (**a**) TEM image and (**b**) HRTEM image of WYO. Reproduced with permission from Ref. [77].

pressing sintering method has been used in the preparation of industrial ITER-grade W bulk materials. Hot isostatic pressing sintering technology can prepare large samples for industrial use, so it has very good application prospects.

Calvo et al. successfully prepared a W–12 wt.% Cr–0.5 wt.% Y alloy with an average grain size of 87 nm by hot isostatic pressing sintering method, and the sintering temperature is 1220 °C. The sintering pressure is 150 MPa, and the sintering time is 2 h. Figure 14 is the SEM image of the W–12 wt.% Cr–0.5 wt.% Y alloy. It can be seen from the SEM image that the second phase is mainly distributed in the GB. The addition of Y can react with oxygen to remove free oxygen and increase the strength of the W–12 wt.% Cr–0.5 wt.% Y alloy [78].

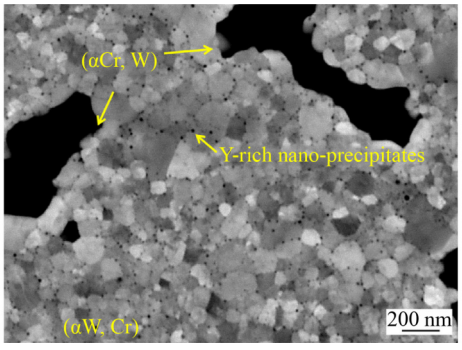

Fig. 14 SEM image of W–12 wt.% Cr–0.5 wt.% Y alloy. Reproduced with permission from Ref. [78].

3.1.3.3 Spark plasma sintering

SPS is also known as plasma-assisted sintering or plasma activated sintering (PAS) [61] that combines energized sintering with hot-press sintering technology. In addition to fast heating speed and short sintering time, SPS also has the characteristics of controllable sintering pressure and temperature and energy-saving capabilities. The SPS device is mainly composed of several parts, including axial pressure device (providing sintering pressure); direct current (DC) pulse power supply (controlling heating rate and sintering temperature); cold punch electrode (used for rapid cooling); vacuum chamber (maintain vacuum); atmosphere control system (provide nitrogen or inert gas); and cooling water, displacement measurement, temperature measurement, safety and security, and other control units. The structure diagram of SPS equipment is shown in Fig. 15 [79].

According to Tokita [80], when a pulsed current is applied to the micro-regions of powder particles, a discharge phenomenon will occur, and this discharge phenomenon will generate plasma. It is generally believed that, in the SPS process, there is Joule heat generated by hot pressing and sintering, and the plastic deformation effect of the material is caused by pressure. In addition to these two effects to promote powder sintering, there will be a DC pulse voltage between the powder particles during the SPS process. The electric discharge phenomenon also occurs between the powder particles, causing the powder to produce a self-heating effect. The parts that are not in contact generate discharge heat, the parts that are in contact generate Joule heat, and the combined effect of the Joule heat generated by the heating of the graphite mold makes the particles' surface melt locally. The high heat on the surface of the particles will cause the bonding parts of the particles to stick together and to form a sintering neck to achieve densification sintering. Compared with other sintering methods, the SPS process has its special effect in favor of sintering. SPS can be widely used in the preparation of special ceramic materials, functionally graded materials,

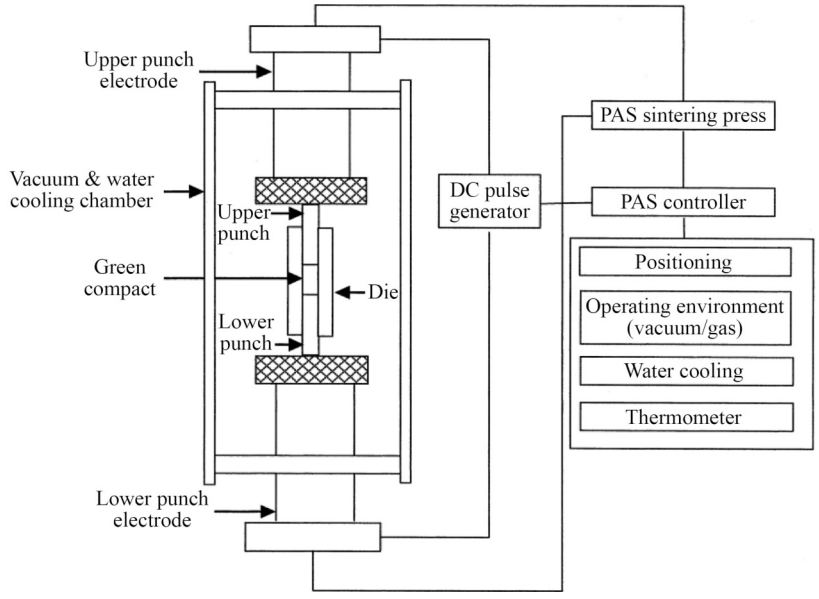

Fig. 15 Structure diagram of the SPS equipment. Reproduced with permission from Ref. [79].

refractory metal materials, nanomaterials, and other fields. Due to the obvious advantages of the SPS sintering technology to prepare bulk materials, it is used in basic research, and great progress has been made in the field of new material applications, nanomaterials, ceramic materials, etc.

Wang et al. successfully prepared a W–1.0% Y_2O_3–0.7% Ti nanocrystalline W alloy material with an average grain size of 67 nm through the SPS technology, as shown in Fig. 16 [81]. Figure 16(a) is the SEM fracture image, and Fig. 16(b) is the grain-size statistics, and it shows that the average grain size of W is 67 nm. The TEM images and size distributions of intragranular and intergranular nanoparticles are shown in Figs. 16(c)–16(f), respectively. The average size of intragranular doped particles is 8.5 nm, and the average size of intergranular doped particles is 16.4 nm (shown in Figs. 16(e) and 16(f), respectively). The sintering temperature is 800 °C for 30 min, 1200 °C for 30 min, and 1400 °C for 5 min with the sintering pressure of 57.3 MPa [81].

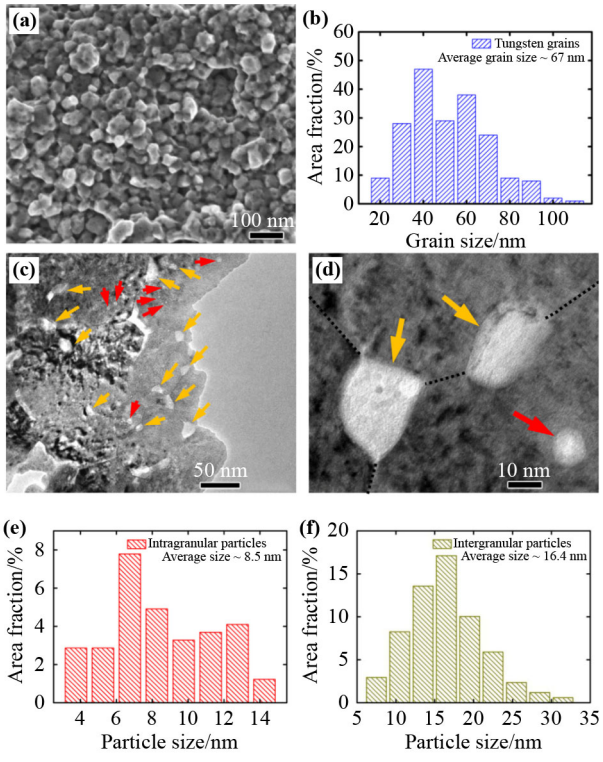

Fig. 16 (**a**) SEM image of fracture surface of W–1.0% Y_2O_3–0.7% Ti, (**b**) grain size distribution of W–1.0% Y_2O_3–0.7% Ti, (**c**)(**d**) TEM images of nanoparticles in W–1.0% Y_2O_3–0.7% Ti, and (**e**)(**f**) size distributions of intragranular and intergranular nanoparticles. Reproduced with permission from Ref. [81].

3.2 Severe plastic deformation (SPD)

3.2.1 High-pressure torsion

Wei et al. prepared a fully dense nanocrystalline W (nc-W) with extremely high strength (~3.0 GPa under quasi-static compression and ~4.0 GPa under dynamic compression) through HPT at a low temperature (500 °C) [82]. Figure 17(a) shows the bright-field TEM image of HPT-W (nominal HPT equivalent strain ~ 70). The grains have an elongated shape, the breakups of the elongated grains are apparent, and many defects appear in W grains.

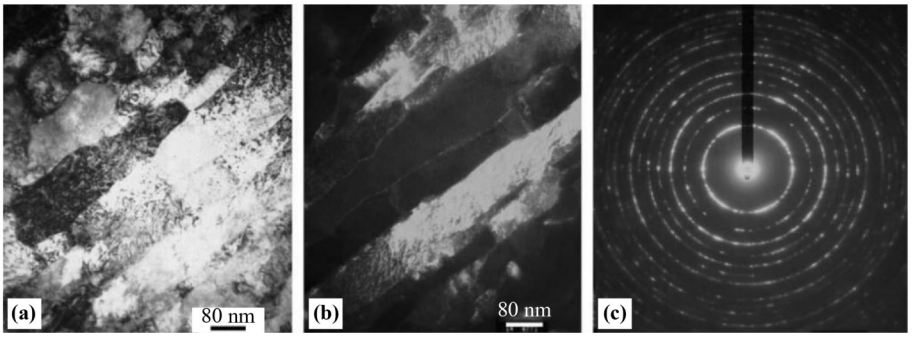

Fig. 17 (**a**) Bright-field image, (**b**) corresponding dark-field image, and (**c**) SAED pattern from HPT-W. Reproduced with permission from Ref. [82].

Figure 17(b) shows the dark-field image, and it also indicates breakups within the elongated grains, and the width of the elongated grains is about 100 nm. Figure 17(c) shows the selected area electron diffraction (SAED) pattern from the region of Fig. 17(a), and the SAED pattern shows nearly continuous rings, and it suggests that the GBs are mostly of the large-angle type.

Kecskes et al. used the HPT method to prepare nanocrystalline W at the temperature of 500 °C, with an imposed pressure of 4 GPa. The total maximum nominal strain in the disk was about 90. The TEM image is shown in Fig. 18. Many defects can be found in the TEM image, and the grains show a long-stripe structure [26].

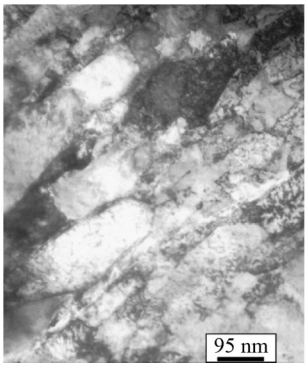

Fig. 18 Bright-field TEM image from a W specimen processed by HPT. Reproduced with permission from Ref. [26].

3.2.2 Surface mechanical attrition treatment

Guo et al. used the SMAT method to prepare a nanocrystalline W–La_2O_3 alloy, and the TEM image and its corresponding dark-field image are shown in Fig. 19 [83]. Elongated W grains can be observed, individual grains with sizes less than 50 nm can be found, and the grains are separated by high-angle GBs. Almost all grains are heavily strained, and a high density of dislocations is present at the grains. The SMAT method is widely used in the preparation of nanocrystalline materials; other nanocrystalline materials, for example, nanocrystalline Al alloys and nanocrystalline Ti–6Al–4V alloy, are also prepared by SMAT [84–86].

ECAE and ARB are the other methods to refine the grain size, and they have shown good application prospects in the field of preparing ultrafine-grained W materials. SMAT and HPT can only be used to prepare small samples. The severe plastic deformation method to prepare nanocrystalline W or W-based materials is not suitable for engineering application.

At present, the powder metallurgy is the most promising

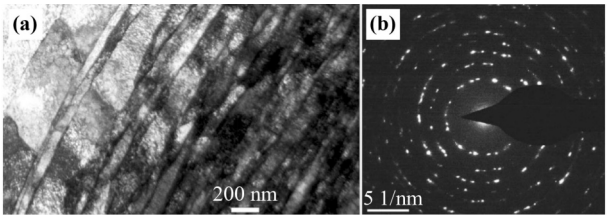

Fig. 19 (**a**) TEM image of the W–La_2O_3 alloy prepared by SMAT and (**b**) corresponding SAED image taken from panel (a). Reproduced with permission from Ref. [83].

method to prepare W-based materials to make the grain size and density of the material meet the demand.

3.3 Challenges and limitations of two methods

The severe plastic deformation method is an effective method for preparing nanocrystalline tungsten materials, and its application still has many challenges and shortcomings. At present, it has been reported that nanocrystalline tungsten materials are prepared by SMAT and HPT methods, and the nanocrystalline tungsten materials prepared by these methods have high density

and no impurity pollution. However, the nanocrystalline tungsten materials prepared by these methods are small and cannot meet the requirements of industrial application. ECAE and ARB can prepare high density materials and have potential for large-scale industrial production. However, they need to be hot rolled at a certain temperature, and it is difficult to prepare nanocrystalline tungsten materials. Further research on the fabrication of nanocrystalline tungsten materials by using severe plastic deformation methods is needed.

The powder metallurgy method is the basic process of raw material powder preparation, powder forming into the required shape of green compact, sintering of green compact, etc. It is especially suitable for preparing refractory metal materials, which can be sintered in vacuum, inert gas and reducing gas, and it is more suitable for preparing nanocrystalline tungsten alloy materials. However, it has the problem of high cost of sintering mold, and the sample size prepared by SPS and RSUHP methods is limited, it cannot meet the industrial application requirements. HIP can prepare large-size samples, and the prepared samples have high density and good uniformity, but the process flow are complex and the cost is high.

4 The properties of nanocrystalline W/W-based materials

Powder metallurgy is the most promising method to prepare nanocrystalline W alloy for engineering applications. Nanocrystalline W alloys were successfully prepared by SPS, HIP, and RSUHP, respectively. Nanocrystalline W films and nanochannel structure W films were prepared by magnetron deposition. Table 1 summarizes the component, preparation method, grain size, relative density, and Vickers hardness of nanocrystalline W alloys or films and commercial pure W [77–78,81,87–88]. Nanocrystalline W alloys possess a large volume percentage of GBs, and they usually show excellent mechanical properties and irradiation-damage resistance.

4.1 Vickers hardness

Nanocrystalline materials possess high Vickers hardness due to their high volume fractions of GBs. Wu et al. [77] prepared nanocrystalline W alloy with an average grain size of 10 nm and tested its Vickers hardness; the results showed that the WYO possessed ultrahigh hardness (1909.3 kgf·mm^{-2}; shown in Table 1), which is much larger than coarse-grained W or W alloys. Figure 20 shows the SEM images of Vickers indents and schematic diagrams of the indentation process of Fig. 20(a) commercial coarse-grained W and Fig. 20(b) sintered WYO. The indents show four pyramid morphologies and different indentation depths (or sizes) for different samples. The higher Vickers hardness of WYO is due to the greater resistance of dislocation motion by the GBs. The schematic diagram shows the GB hardening through dislocation pileup and the dispersion strengthening by second-phase particle pinning.

Wang et al. [81] prepared W–1 wt.% Y_2O_3–0.7 wt.% Ti (WYT) by SPS, with an average grain size of 67 nm, as shown in Table 1. The Vickers hardness is 1441 kgf·mm^{-2}, and its Vickers impression was shown in Fig. 21. Calvo et al. [78] prepared W–12 wt.% Cr–0.5 wt.% Y (WCY) by HIP, with an average grain size of 87 nm, as shown in Table 1, and the Vickers hardness is 1228 kgf·mm^{-2}. The Vickers hardness of nanocrystalline W alloys is much higher than that of the coarse-grained pure W.

The high hardness of nanocrystalline W alloys originates from the high volume fraction of GBs and the dispersion of the second phase. The essence of the GB

Table 1 The component, preparation method, grain size, relative density, and Vickers hardness of commercial pure W and nanocrystalline W alloys or films [77–78,81,87–88]

Material	Preparation method	d/nm	ρ_r/%	VH/(kgf·mm^{-2})	Ref.
W–5 wt.% Y_2O_3 (WYO)	RSUHP	10	94.1	1909.3	[77]
W–1 wt.% Y_2O_3–0.7 wt.% Ti (WYT)	SPS	67	98.6	1441	[81]
W–12 wt.% Cr–0.5 wt.% Y (WCY)	HIP	87	99	1228	[78]
Pure W (PW)	HIP	2296	99.7	487	[77]
Nanochannel W films	magnetron deposition	64.2–168.4	–	–	[87]
35 nm nanocrystalline W film	magnetron deposition	35	–	–	[88]

Notes: d, grain size; ρ_r, relative density; VH, Vickers hardness.

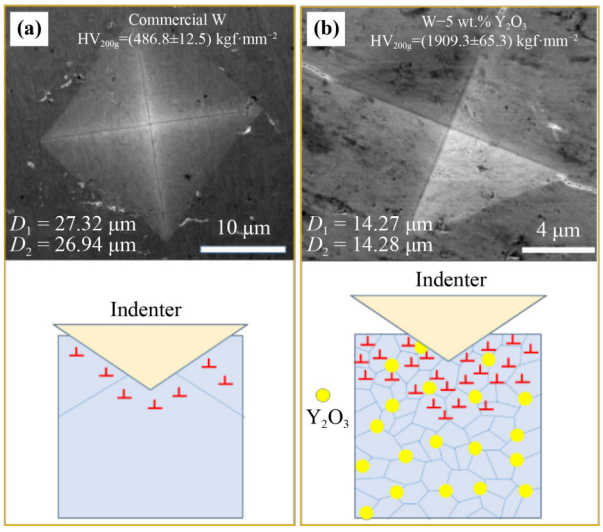

Fig. 20 SEM images of Vickers indentation and schematic diagrams of the indentation process of (**a**) commercial coarse-grained W and (**b**) sintered WYO. The yellow circle spots represent the Y_2O_3 grains while the red symbols '⊥' represent the dislocations. Reproduced with permission from Ref. [77].

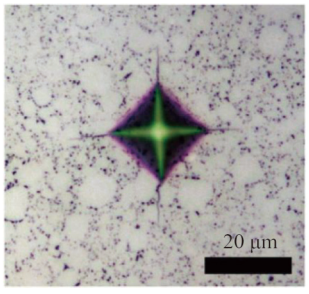

Fig. 21 An optical graph showing the Vickers impression of the WYT sample. Reproduced with permission from Ref. [81].

hardening mechanism is to prevent the movement of dislocations. Dislocation clusters are formed in front of the GB and sub-GB when dislocations encounter obstacles in motion and external forces are insufficient to overcome obstacles. Dislocation plugs are formed, and they impede the movement of dislocations and improve the hardness of materials. The secondary-phase nanoparticles can inhibit the growth of matrix grains, and improve the volume fraction of GBs. Furthermore, the secondary-phase nanoparticles can promote the homogenization of tungsten grain size, and this uniform microstructure is beneficial to improve the strength of materials [89–90]; the interfaces can also act as a potential barrier to hinder the movement of dislocations and play the role of dispersion strengthening, that is, the hardening effect of the secondary-phase particles.

4.2 Irradiation behavior of nanocrystalline or nanostructured W/W-based materials

The service environment of PFMs includes high-energy neutron irradiation; low-energy, high-flux D/T + 5% He plasma irradiation; and other particle streams coordinated irradiation, and these irradiations can cause damage to materials. Many simulations and experimental research studies on H, D, He, and heavy ion irradiation of nanocrystalline or nanostructured W were reported [77,87–88,91–101].

4.2.1 He ion irradiation behavior

W materials in a fusion reactor facing plasma and neutron irradiation and the irradiation performance of nanocrystalline W alloys deserve to be studied. Wu et al. [77] conducted high-temperature He^+ ion irradiation experiments on NEC 400 kV ion implanter. The He^+ ion doses are 2×10^{17}, 5×10^{17}, and 1×10^{18} ions·cm^{-2} with an irradiation temperature of 450 °C and the dose rate of 4.85×10^{13} ions·cm^{-2}·s^{-1}, respectively. The bright-field TEM images of low magnification and high magnification at three irradiation doses are shown in Fig. 22, respectively. The interest depths of irradiated W and WYO are 534 and 570 nm, respectively. The bubble areal density was counted and calculated, and the swelling was also obtained and calculated.

The swelling and bubble areal density of coarse-grained pure W and nanocrystalline WYO increase with the increase of irradiation dose. Under the three irradiation doses, the swelling and bubble areal density of nanocrystalline WYO are lower than those of coarse-grained pure W. Under the irradiation dose of 2×10^{17} ions·cm^{-2}, the swelling of coarse-grained pure W is about three times that of nanocrystalline WYO. The nanocrystalline WYO shows excellent irradiation swelling resistance performance, because nanocrystalline WYO has a smaller grain size and a higher volume fraction of GBs and interfaces, providing a large number of vacancies for the absorption of He atoms; at the same time, the GBs and interfaces can be used as the escape channels of He atoms in the material and allow He atoms in the material to escape from the surface of the sample. In addition, the high-temperature irradiation conditions make the vacancies easy to migrate, which enhances the absorption and transfer of He atoms to the surface of the sample through the GB and interface.

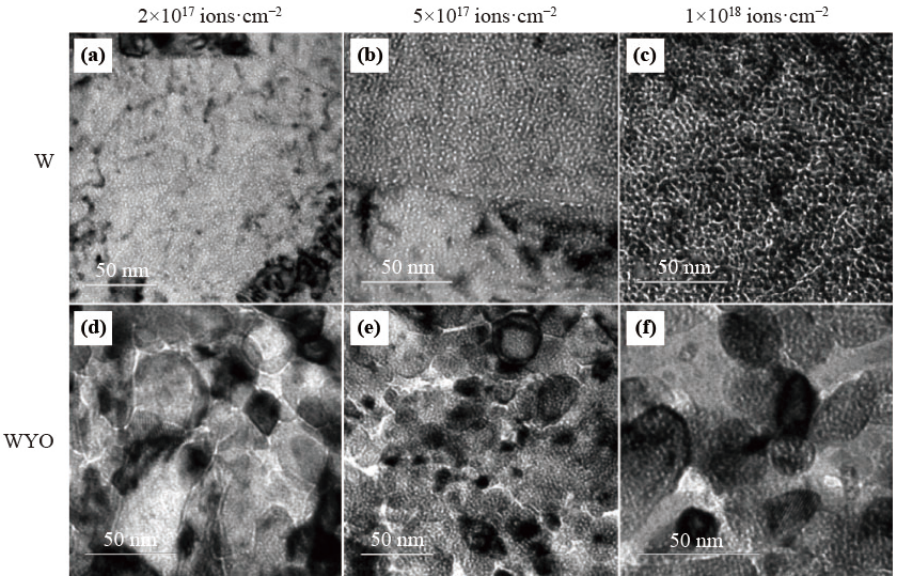

Fig. 22 High-magnification bright-field TEM images of 120 keV He^+ irradiated samples at different doses: (**a**) W, 2×10^{17} ions·cm^{-2}; (**b**) W, 5×10^{17} ions·cm^{-2}; (**c**) W, 1×10^{18} ions·cm^{-2}; (**d**) WYO, 2×10^{17} ions·cm^{-2}; (**e**) WYO, 5×10^{17} ions·cm^{-2}; (**f**) WYO, 1×10^{18} ions·cm^{-2}. Reproduced with permission from Ref. [77].

Qin et al. [87] prepared nanochannel W films with different nanochannel densities on silicon (1 0 0) substrates, using ultrahigh vacuum DC magnetron sputtering deposition at different experiment conditions, and conducted high-energy He^+ ion irradiation experiments on nanochannel W films and bulk W at RT; the energy of He^+ ion was 40 keV, and the fluences was up to 10^{18} ions·cm^{-2}. The cross-sectional transmission electron microscopy (XTEM) images of the irradiated nanochannel W films and bulk W are shown in Fig. 23, and the average columnar sizes in the nanochannel W-RT-150W, W-600-150W, and W-600-50W films are approximately 64.2, 92.9, and 168.4 nm, respectively, and the nanochannel W-600-50W film contains the fewest number of nanochannels [87].

Figure 24 shows the average bubble size and the areal density of the samples irradiated to different fluences measured from the TEM images [87]. The average bubble size of bulk materials is slightly larger than that in the nanochannel W films, and the bubble areal density of bulk materials is much larger than that in the nanochannel W films at the same fluence. The average bubble size increases with the increase of the nanochannel density, while the bubble areal density decreases. The changes of average bubble size and bubble areal density reveal that the He bubble concentration in W films decreases with the increase of nanochannel density, and they are much lower than those found in bulk W. The results show that abundant free surfaces in nanochannel W films can act as "sinks", and they trap the He atoms and release He atoms to the surface through the nanochannels. The He bubble formation was retarded in the nanochannel W films compared with the bulk W, and the nanochannel W films possess a high irradiation tolerance and "self-healing" capability.

El-Atwani et al. [101] conducted helium irradiation experiments at the Microscope and Ion Accelerator for Materials Investigations (MIAMI) facility. The irradiation temperature is 1223 K, and the energy of helium is 2 keV with the fluence rate of 3.3×10^{12} ions·cm^{-2}·s^{-1}. The energy of helium is sufficient to induce atomic displacement, and the vacancies and interstitials are generated and can be able to migrate. Figure 25 shows the bright-field TEM images of ultrafine grained (UFG) and nanocrystalline (NC) tungsten irradiated with 2 keV helium ions at 1223 K; the results show that bubbles with different sizes were uniformly distributed across the grains, and smaller nanocrystalline grains possess lower areal densities. Irradiation defects on ultrafine grains and the lower areal density of bubbles on nanocrystalline grains were observed. Large and facetted cavities can be found at the GBs of nanocrystalline grains, and this phenomenon demonstrates the better helium sink efficiency of nanocrystalline W materials, and the degradation of mechanical properties may be possible as a result of bubbles' formation.

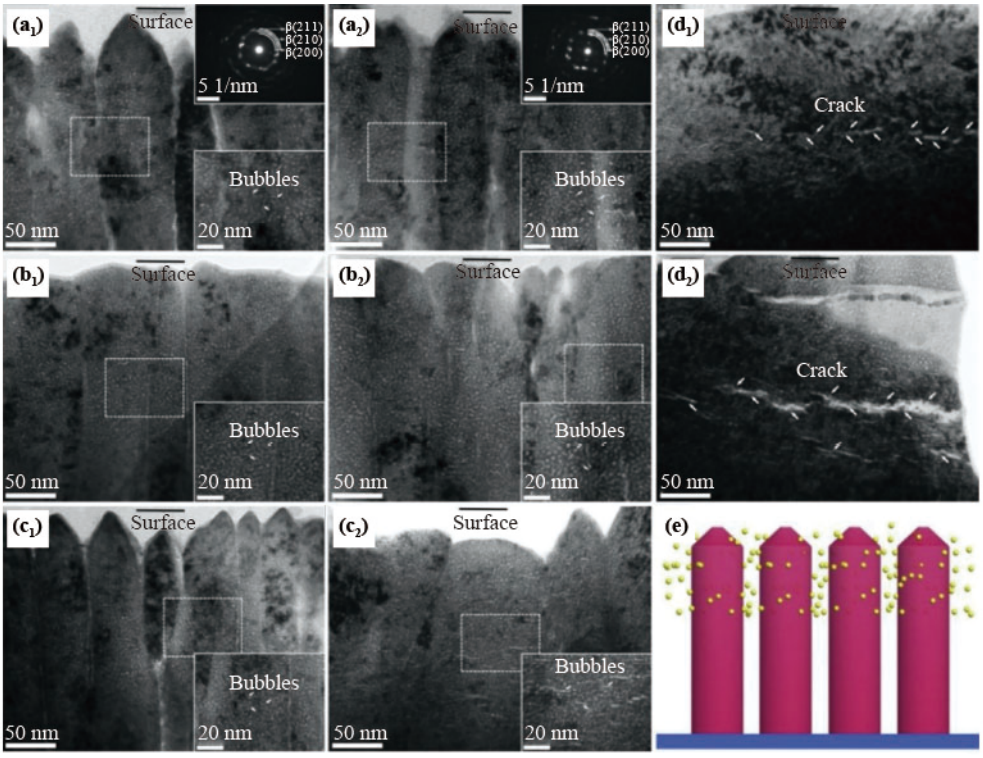

Fig. 23 XTEM images of the irradiated nanochannel W films and bulk W to the fluence of (**a**$_1$)(**b**$_1$)(**c**$_1$)(**d**$_1$) 5×10^{17} ions·cm^{-2} and (**a**$_2$)(**b**$_2$)(**c**$_2$)(**d**$_2$) 1×10^{18} ions·cm^{-2} (nanochannel films: W-RT-150W (panels (a_1) and (a_2)); W-600-150W (panels (b_1) and (b_2)); W-600-50W (panels (c_1) and (c_2)); bulk W (panels (d_1) and (d_2)). (**e**) Diffusion model of He bubbles (yellow ball) in the nanochannel W films (deep pink column). The SAED patterns of W-RT-150 W is inserted in the upper right of panels (a_1) and (a_2). Reproduced with permission from Ref. [87].

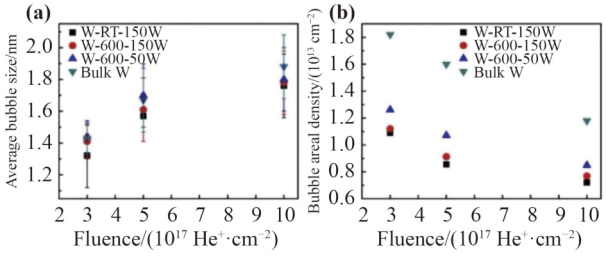

Fig. 24 Statistical results of the average bubble size and bubble areal density in the irradiated samples: (**a**) average bubble size and (**b**) bubble areal density of nanochannel films W-RT-150W, W-600-150W, W-600-50W, and bulk W as a function of fluence. Reproduced with permission from Ref. [87].

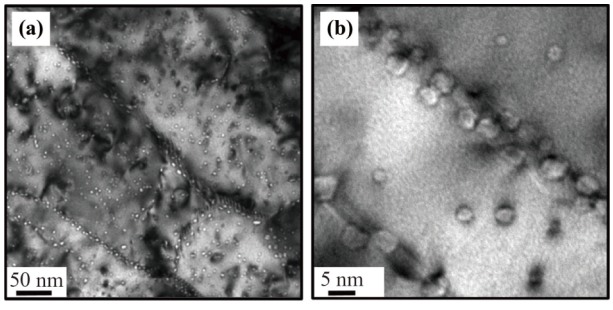

Fig. 25 Bright-field TEM images of UFG and NC tungsten irradiated by 2 keV helium ions at 1223 K: (**a**) overview of sample with bubbles distributed at GBs with irradiation fluence of 3.6×10^{15} ions·cm^{-2}; and (**b**) nanocrystalline grain with large facetted bubbles/voids on GBs and few bubbles in the grain matrix at irradiation fluence of 3.6×10^{15} ions·cm^{-2}. Reprinted with permission from Ref. [101].

Nanocrystalline W alloys possess excellent irradiation resistance compared with coarse-grained W due to its high volume fraction of GBs or free surfaces, and the GBs or free surfaces act as "sinks" to trap He atoms; furthermore, they are also act as releasing channel for He atoms to transfer from interior to surface of materials.

4.2.2 Heavy ion irradiation behavior

Plasma-facing materials face high-energy (14.1 MeV) neutron irradiation, and heavy ion irradiation was used to simulate neutron irradiation, as there are few institutions that can conduct neutron irradiation experiments. The dpa (displacement per atom) of materials caused by heavy ion irradiation can be simulated by the SRIM (Stopping and Range of Ions in Matter).

El-Atwani et al. [88] prepared nanocrystalline W

(NCW) film via magnetron deposition from a W target of 99.99% purity. The deposition was performed at RT, using 100 W DC power and 4 mTorr pressure. The thickness of NCW film is 100 nm, and the grain size is 35 nm obtained from TEM image. The *in situ* Kr ion irradiation experiment was conducted on 35 nm NCW, and the energy of Kr^{2+} was 1 MeV; the irradiation experiment was performed by using the intermediate voltage electron microscope (IVEM) attached to a Tandem accelerator at Argonne National Laboratory.

Figure 26 shows the snapshots of bright-field TEM micrographs taken from an *in situ* irradiation experiment at ~0.42 dpa, showing loop absorption by the GBs in the NCW-35 nm irradiated with 1 MeV Kr^{2+} at room temperature (RT) [88]. The NCW-35 nm sample exhibited continuous and rapid loop absorption by the GBs, which could be observed only through TEM by the *in situ* irradiation experiments. The microstructural damage of dislocation loop can be obtained under a specific two-beam condition. In a typical TEM image, some dislocation loops are invisible at $\boldsymbol{g}\cdot\boldsymbol{b} = 0$, where $\boldsymbol{g}$ is the diffraction vector, and $\boldsymbol{b}$ is the burgers vector of the loop. The details about the imaging methods for dislocation loops are introduced in Ref. [100], and more information about the two-beam condition technology can be found in Refs. [102–105]. Figure 26 shows loop annihilation after nucleation by the GBs (the loops are marked with red arrows, and then the loops are absorbed by the GBs).

Figure 27 shows the snapshots bright-field TEM micrographs taken from an *in situ* irradiation experiment at ~8 dpa, and it shows loop absorption by the GBs in the same grain in the NCW-35 nm irradiated with 1 MeV Kr^{2+} at 1073 K [88]. The rapid annihilation by ~35 nm grains at a higher dose and higher temperature is shown in Fig. 27. The results show that the number of loops remained the same during 43 s of irradiation, and the nucleation of loops by irradiation and the absorption of loops by GBs reach a balance. The overall damage (up to 10 dpa) in the NCW-35 nm sample at 1073 K shows nearly no change. Post high-temperature and high-dose irradiation examination showed an order-of-magnitude decrease in the damage. Loop migration to GBs continues when there is a high temperature after the irradiation is stopped, and the high volume fraction of GBs of nanocrystalline W materials can act as storage for accumulating further defects and improve the irradiation tolerance.

The reported research results on the properties of nanocrystalline W/W-based materials may help us further understand and grasp the mechanism and the influence of grain size on material properties and clarify the role and mechanism of GBs on the mechanical properties of materials. The physical mechanism of the interaction between GBs and defects (such as off-site damage, vacancies, and loops caused by irradiation) was revealed. Nanocrystalline tungsten alloy materials possess excellent mechanical properties and high resistance to irradiation damage, as illustrated by the experimental and simulation

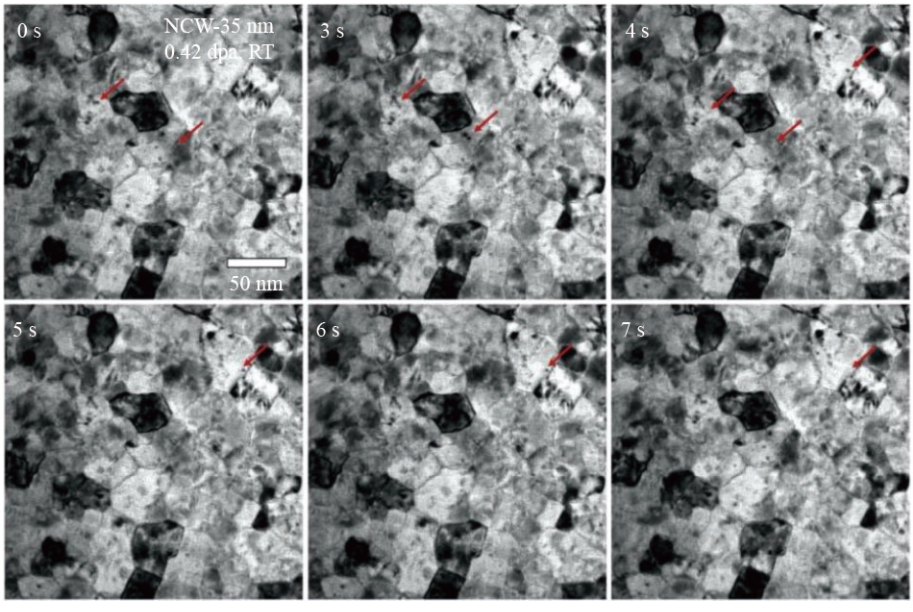

Fig. 26 Snapshots of bright-field TEM micrographs taken from an *in situ* irradiation experiment at ~0.42 dpa showing loop absorption by the GBs in the NCW-35 nm irradiated with 1 MeV Kr^{2+} at RT. Reproduced with permission from Ref. [88].

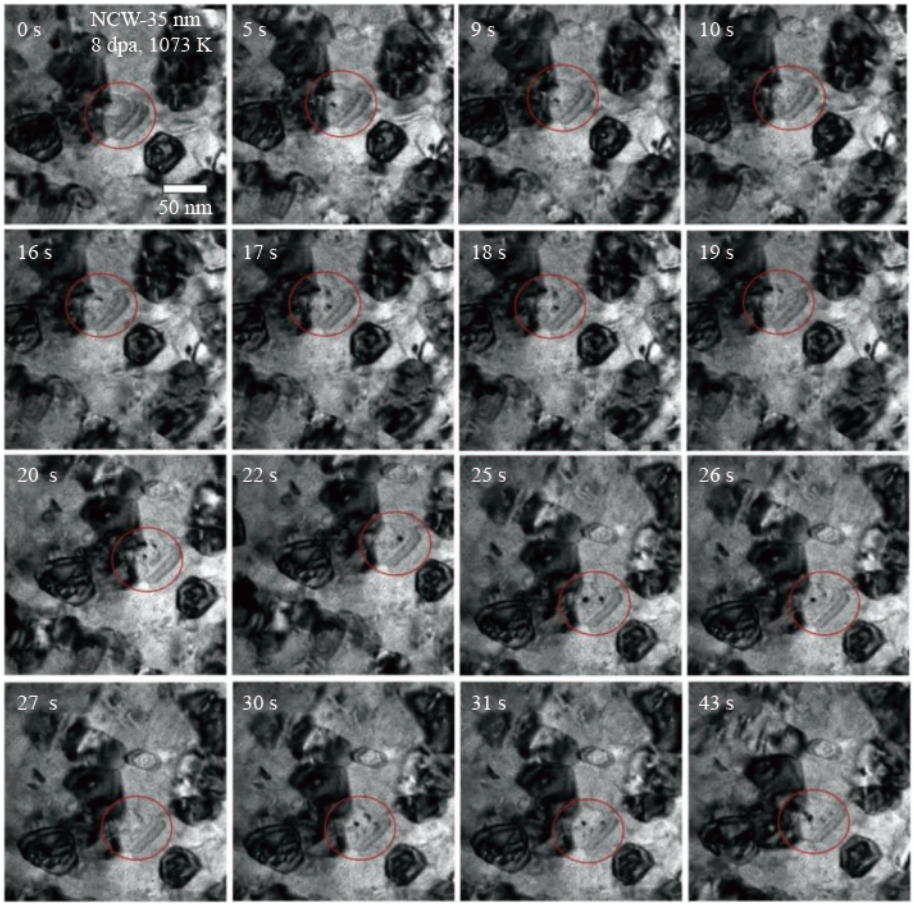

Fig. 27 Snapshots of bright-field TEM micrographs taken from an *in situ* irradiation experiment at ~8 dpa showing loop absorption by the GBs in the same grain in the NCW-35 nm irradiated with 1 MeV Kr^{2+} at 1073 K. Reproduced with permission from Ref. [88].

results. However, as a plasma-facing materials, the comprehensive properties of W/W-based materials should be considered, such as thermal conductivity, retention problem, thermal stability, and thermal shock performance. Research on the above properties and problems needs to be further studied and explored in the future in order to obtain high-performance plasma-facing nanocrystalline W/W-based materials that meet the application conditions of a fusion reactor.

5 Conclusions

The research and development of nanocrystalline W/W-based materials were reviewed. Theoretical guidance for the preparation of nanocrystalline W/W-based materials was provided, and several novel approaches were successfully adopted to prepare nanocrystalline W/W-based materials, including bottom-up methods, such as SPS, HIP, and RSUHP, and top-down methods, such as HPT and SMAT. The preparation of nanocrystalline W powder through processes such as the wet-chemical method and high-energy ball milling plays a vital role in the preparation of nanocrystalline W/W-based materials, as well as the secondary-phase particles mechanical alloyed with W powder to prevent the grain growth during the sintering process.

The excellent mechanical property of nanocrystalline W-based materials comes from GB hardening and dispersion hardening. The essence of the GB hardening mechanism is that GBs act as obstacles and prevent the movement of dislocations. More external forces are required to overcome obstacles and lead to the increase of hardness; furthermore, the secondary-phase particles act as pinning points to hinder the movement of dislocations. The unexpected irradiation tolerance of nanocrystalline W/W-based materials comes from the large volume percentage of GBs and free surfaces, and the GBs or free surfaces act as absorption “sinks” to trap He atoms and defects; furthermore, they also act as releasing channels for He atoms to transfer from the interior to the surface of materials.

Nanocrystalline W/W-based materials are very difficult to prepare due to their high melting point and low recrystallization temperature, and nanocrystalline W/W-based materials possess excellent mechanical properties and unexpected irradiation tolerance, and they may solve the problems of pure W that restrict the industrial application. Nanocrystalline W-based materials are one of the most promising PFMs, due to their high performance, which deserves further research and investigation.

Authors' contribution Conceptualization, Z.W. and Q.L.; methodology, Z.W. and X.Y.; software, Z.W.; validation, Z.W. and Q.L.; formal analysis, Q.L.; investigation, X.Y.; resources, Z.W.; data curation, Q.L. and X.Y.; writing (original draft preparation), Z.W.; writing (review and editing), Q.L. and X.Y.; visualization, Z.W. and Q.L.; supervision, Q.L.; project administration, Z.W.; funding acquisition, Z.W. All authors have read and agreed to the published version of the manuscript.

Disclosure of potential conflict of interest The authors declare no competing interest.

Acknowledgements This work was funded by the National Natural Science Foundation of China (Grant No. 12105254).

References

[1] Sauthoff N R U S. Contributions to ITER. Fusion Engineering and Design, 2006, 81: 87–92

[2] Klein F, Litnovsky A, Tan X, et al. Smart alloys as armor material for DEMO: overview of properties and joining to structural materials. Fusion Engineering and Design, 2021, 166: 112272

[3] Claessens M. ITER: The Giant Fusion Reactor — Bringing a Sun to Earth. Springer, 2019

[4] Cui S, Zhang D, Lang Y, et al. A new method for improving the tritium breeding and releasing performance of China Fusion Engineering Test Reactor phase II helium-cooled ceramic breeder blanket. International Journal of Energy Research, 2020, 44: 5977–5989

[5] Conte M, Aktaa J. Manufacturing influences on microstructure and fracture mechanical properties of polycrystalline tungsten. Nuclear Materials and Energy, 2019, 21: 100591

[6] Philipps V. Tungsten as material for plasma-facing components in fusion devices. Journal of Nuclear Materials, 2011, 415: S2–S9

[7] Hasegawa A, Fukuda M, Yabuuchi K, et al. Neutron irradiation effects on the microstructural development of tungsten and tungsten alloys. Journal of Nuclear Materials, 2016, 471: 175–183

[8] Zinkle S J, Snead L L. Designing radiation resistance in materials for fusion energy. Annual Review of Materials Research, 2014, 44: 241–267

[9] Knaster J, Moeslang A, Muroga T. Materials research for fusion. Nature Physics, 2016, 12: 424–434

[10] Li Y G, Zheng Q R, Wei L M, et al. A review of surface damage/microstructures and their effects on hydrogen/helium retention in tungsten. Tungsten, 2020, 2: 34–71

[11] Xiao S, Ma Y, Tian L, et al. Decrease of blistering on Helium irradiated tungsten surface via transversal release of helium from the grooved surfaces. Nuclear Materials and Energy, 2020, 23: 100746

[12] Meyer F W, Han L, Hijazi H, et al. Energy dependence of He-ion-induced tungsten nanofuzz formation at non-normal incidence angles. Nuclear Materials and Energy, 2017, 12: 366–371

[13] Dasgupta D, Kolasinski R D, Friddle R W, et al. On the origin of 'fuzz' formation in plasma-facing materials. Nuclear Fusion, 2019, 59: 086057

[14] Yuan Y, Wang T, Kreter A, et al. Influence of neon seeding on the deuterium retention and surface modification of ITER-like forged tungsten. Nuclear Fusion, 2020, 61: 016007

[15] Yan Q Z, Zhang X F, Zhou Z J, et al. Status of R&D on plasma facing materials in China. Journal of Nuclear Materials, 2013, 442: S190–S197

[16] Sun Z, Diallo A, Maingi R, et al. Suppression of edge localized modes with real-time boron injection using the tungsten divertor in EAST. Nuclear Fusion, 2021, 61: 014002

[17] Giannattasio A, Yao Z, Tarleton E, et al. Brittle–ductile transitions in polycrystalline tungsten. Philosophical Magazine, 2010, 90(30): 3947–3959

[18] Roth J, Schmid K. Hydrogen in tungsten as plasma-facing material. Physica Scripta, 2011, T145: 014031

[19] Alimov V K, Roth J. Hydrogen isotope retention in plasmafacing materials: review of recent experimental results. Physica Scripta, 2007, T128: 6

[20] Meyers M A, Mishra A, Benson D J. Mechanical properties of nanocrystalline materials. Progress in Materials Science, 2006, 51: 427–556

[21] Zhao Y H, Topping T, Bingert J F, et al. High tensile ductility and strength in bulk nanostructured nickel. Advanced Materials, 2008, 20: 3028–3033

[22] Zhou Q, Zhao J, Xie J Y, et al. Grain size dependent strain rate sensitivity in nanocrystalline body-centered cubic metal thin films. Materials Science and Engineering A, 2014, 608: 184–189

[23] Grimes R W, Konings R J M, Edwards L. Greater tolerance for nuclear materials. Nature Materials, 2008, 7(9): 683–685

[24] Ackland G. Controlling radiation damage. Science, 2010, 327: 1587–1588

[25] Li X, Liu W, Xu Y C, et al. An energetic and kinetic

perspective of the grain boundary role in healing radiation damage in tungsten. Nuclear Fusion, 2013, 53: 123014

[26] Kecskes L, Cho K, Dowding R, et al. Grain size engineering of bcc refractory metals: top-down and bottom-up-application to tungsten. Materials Science and Engineering A, 2007, 467: 33–43

[27] Hao T, Fan Z, Zhao S, et al. Microstructures and properties of ultrafine-grained tungsten produced by equal-channel angular pressing at low temperatures. Journal of Nuclear Materials, 2013, 433: 351–356

[28] Ameyama K, Oda E, Fujiwara H. Superplasticity and high temperature deformation behaviour in nano grain tungsten compacts. Materialwissenschaft and Werkstofftechnik, 2008, 39(4–5): 336–339

[29] Shkodich N, Spasova M, Farle M, et al. Structural evolution and magnetic properties of high-entropy CuCrFeTiNi alloys prepared by high-energy ball milling and spark plasma sintering. Journal of Alloys and Compounds, 2020, 816: 152611

[30] Oda E, Fujiwara H, Ameyama K. Nano grain formation in tungsten by severe plastic deformation-mechanical milling process. Materials Transactions, 2008, 49: 54–57

[31] Xia M, Yan Q Z, Xu L, et al. Bulk tungsten with uniformly dispersed La_2O_3 nanoparticles sintered from co-precipitated La_2O_3/W nanoparticles. Journal of Nuclear Materials, 2013, 434: 85–89

[32] Xia M, Yan Q, Xu L, et al. Synthesis of TiC/W core–shell nanoparticles by precipitate-coating process. Journal of Nuclear Materials, 2012, 430: 216–220

[33] Xu L, Yan Q, Xia M, et al. Preparation of La_2O_3 doped ultra-fine W powders by hydrothermal-hydrogen reduction process. International Journal of Refractory Metals & Hard Materials, 2013, 36: 238–242

[34] Dias M, Guerreiro F, Correia J B, et al. Consolidation of W–Ta composites: hot isostatic pressing and spark and pulse plasma sintering. Fusion Engineering and Design, 2015, 98–99: 1950–1955

[35] Kim H G, Kim K T. Densification behavior of tungsten-fiber-reinforced copper powder compacts under hot isostatic pressing. International Journal of Mechanical Sciences, 2000, 42: 1339–1356

[36] Weber T, Zhou Z, Qu D, et al. Resistance sintering under ultra high pressure of tungsten/EUROFER97 composites. Journal of Nuclear Materials, 2011, 414: 19–22

[37] Qu D, Zhou Z, Tan J, et al. Characterization of W/Fe functionally graded materials manufactured by resistance sintering under ultra-high pressure. Fusion Engineering and Design, 2015, 91: 21–24

[38] Choi J, Sung H M, Roh K B, et al. Fabrication of sintered tungsten by spark plasma sintering and investigation of thermal stability. International Journal of Refractory Metals & Hard Materials, 2017, 69: 164–169

[39] Zhou Y F, Zhao Z Y, Tan X Y, et al. Densification and microstructure evolution of W–TiC–Y_2O_3 during spark plasma sintering. International Journal of Refractory Metals & Hard Materials, 2019, 79: 95–101

[40] Fan Z S, Xiang D P, Pan Y L, et al. Effect of two-time spark plasma sintering on microstructure and mechanical properties of W–6Ni–4Mn alloy. Materials Science and Engineering A, 2019, 745: 300–306

[41] Huang L, Jiang L, Topping T D, et al. *In situ* oxide dispersion strengthened tungsten alloys with high compressive strength and high strain-to-failure. Acta Materialia, 2017, 122: 19–31

[42] Yar M A, Wahlberg S, Bergqvist H, et al. Spark plasma sintering of tungsten–yttrium oxide composites from chemically synthesized nanopowders and microstructural characterization. Journal of Nuclear Materials, 2011, 412: 227–232

[43] Liu R, Xie Z M, Fang Q F, et al. Nanostructured yttria dispersion-strengthened tungsten synthesized by sol-gel method. Journal of Alloys and Compounds, 2016, 657: 73–80

[44] Prabhu G, Chakraborty A, Sarma B. Microwave sintering of tungsten. International Journal of Refractory Metals & Hard Materials, 2009, 27: 545–548

[45] Prabhu G, Kumar N A, Sankaranarayana M, et al. Tensile and impact properties of microwave sintered tungsten heavy alloys. Materials Science and Engineering A, 2014, 607: 63–70

[46] Ma Y, Zhang J, Liu W, et al. Microstructure and dynamic mechanical properties of tungsten-based alloys in the form of extruded rods via microwave heating. International Journal of Refractory Metals & Hard Materials, 2014, 42: 71–76

[47] Krywopusk N M, Kecskes L J, Weihs T P. The effect of strain rate on the microstructural evolution of pure Mg during ECAE. Materials Characterization, 2021, 178: 111209

[48] Valiev R Z, Korznikov A V, Mulyukov R R. Structure and properties of ultrafine-grained materials produced by severe plastic deformation. Materials Science and Engineering A, 1993, 168: 141–148

[49] As A, Mwv A, Bma B, et al. Tube equal channel angular extrusion (tECAE) of Mg–3Al–1Zn alloy. Materials Science and Engineering A, 2021, 814: 141236

[50] Edalati K, Toh S, Watanabe M, et al. *In situ* production of bulk intermetallic-based nanocomposites and nanostructured intermetallics by high-pressure torsion. Scripta Materialia, 2012, 66: 386–389

[51] Yan B, Estrin Y, Mazilkin A, et al. Quantifying solid-state mechanical mixing by high-pressure torsion. Journal of Alloys and Compounds, 2021, 878: 160419

[52] Zhou L, Liu G, Ma X L, et al. Strain-induced refinement in a steel with spheroidal cementite subjected to surface mechanical attrition treatment. Acta Materialia, 2008, 56: 78–87

[53] Wu X L, Tao N R, Wei Q M, et al. Microstructural evolution and formation of nanocrystalline intermetallic compound during surface mechanical attrition treatment of cobalt. Acta Materialia, 2007, 55: 5768–5779

[54] Lu K, Lu J. Nanostructured surface layer on metallic materials induced by surface mechanical attrition treatment. Materials Science and Engineering A, 2004, 375–377: 38–45

[55] Tsuji N, Saito Y, Utsunomiya H, et al. Ultra-fine grained bulk steel produced by accumulative roll-bonding (ARB). Scripta Materialia, 1999, 40(7): 795–800

[56] Tsuji N, Ito Y, Saito Y, et al. Strength and ductility of ultrafine grained aluminum and iron produced by ARB and annealing. Scripta Materialia, 2002, 47(12): 893–899

[57] Lang S, Yan Q, Wang Y, et al. Preparation and microstructure characterization of W–0.1 wt.% TiC alloy via chemical method. International Journal of Refractory Metals & Hard Materials, 2016, 55: 33–38

[58] Zhang X, Wu X, Hou C. First-principles calculations on interface stability and migration of H and He in W–ZrC interfaces. Applied Surface Science, 2020, 499: 143995

[59] Xie Z M, Liu R, Miao S, et al. High thermal shock resistance of the hot rolled and swaged bulk W–ZrC alloys. Journal of Nuclear Materials, 2016, 469: 209–216

[60] Tan X Y, Luo L M, Lu Z L, et al. Development of tungsten as plasma-facing materials by doping tantalum carbide nanoparticles. Powder Technology, 2015, 269: 437–442

[61] Miao S, Xie Z M, Yang X D, et al. Effect of hot rolling and annealing on the mechanical properties and thermal conductivity of W–0.5 wt.% TaC alloys. International Journal of Refractory Metals & Hard Materials, 2016, 56: 8–17

[62] Zhang X, Yan Q, Lang S, et al. Evolution of hot rolling texture in pure tungsten and lanthanum oxide doped tungsten with various reductions. Materials & Design, 2016, 109: 443–455

[63] Xie Z M, Liu R, Zhang T, et al. Achieving high strength/ductility in bulk W–Zr–Y_2O_3 alloy plate with hybrid microstructure. Materials & Design, 2016, 107: 144–152

[64] El-Atwania O, Quach D V, Efe M, et al. Multimodal grain size distribution and high hardness in fine grained tungsten fabricated by spark plasma sintering. Materials Science and Engineering A, 2011, 528(18): 5670–5677

[65] Wang S, Sun C, Guo W, et al. Modifying the properties of tungsten based plasma facing materials with single-wall carbon nanotubes. Journal of Materials Science and Technology, 2013, 29: 919–922

[66] Zhang L H, Jiang Y, Fang Q F, et al. Toughness and microstructure of tungsten fibre net-reinforced tungsten composite produced by spark plasma sintering. Materials Science and Engineering A, 2016, 659: 29–36

[67] Fu T, Cui K, Zhang Y, et al. Oxidation protection of tungsten alloys for nuclear fusion applications: a comprehensive review. Journal of Alloys and Compounds, 2021, 884: 161057

[68] Fu T, Shen F, Zhang Y, et al. Oxidation protection of high-temperature coatings on the surface of Mo-based alloys — a review. Coatings, 2022, 12(2): 141

[69] Zhang Y, Fu T, Yu L, et al. Anti-corrosion coatings for protecting Nb-based alloys exposed to oxidation environments: a review. Metals and Materials International, 2023, 29: 1–17

[70] Shen F, Zhang Y, Yu L, et al. Microstructure and oxidation behavior of Nb–Si-based alloys for ultrahigh temperature applications: a comprehensive review. Coatings, 2021, 11(11): 1373

[71] Chookajorn T, Heather A, Murdoch C, et al. Design of stable nanocrystalline alloys. Science, 2012, 337: 951–954

[72] Zhang Y, Yu L, Fu T, et al. Microstructure evolution and growth mechanism of Si–$MoSi_2$ composite coatings on TZM (Mo–0.5Ti–0.1Zr–0.02C) alloy. Journal of Alloys and Compounds, 2021, 894(15): 162403

[73] Zhang Y, Fu T, Yu L, et al. Improving oxidation resistance of TZM alloy by deposited Si–$MoSi_2$ composite coating with high silicon concentration. Ceramics International, 2022, 48(14): 20895–20904

[74] Zhang Y, Laiho Yu, Tao F, et al. Microstructure and oxidation resistance of Si–$MoSi_2$ ceramic coating on TZM (Mo–0.5Ti–0.1Zr–0.02C) alloy at 1500 °C. Surface and Coatings Technology, 2022, 431(15): 128037

[75] Wu Z M, Liang Y X, Fan Y, et al. The ball to powder ratio (BPR) dependent morphology and microstructure of tungsten powder refined by ball milling. Powder Technology, 2018, 339: 256–263

[76] Liu G, Zhang G, Jiang F, et al. Nanostructured high-strength molybdenum alloys with unprecedented tensile ductility. Nature Materials, 2013, 12: 344–350

[77] Wu Z M, Zhang J, Zhang J, et al. Nanocrystalline W-based alloys with ultrahigh hardness and exceptional irradiation tolerance. Nuclear Fusion, 2019, 59(10): 106050

[78] Calvo A, García-Rosales C, Koch F, et al. Manufacturing and testing of self-passivating tungsten alloys of different composition. Nuclear Materials and Energy, 2016, 9: 422–429

[79] Jung Y G, Ha C G, Shin J H, et al. Fabrication of functionally graded ZrO_2/NiCrAlY composites by plasma activated sintering using tape casting and its thermal barrier property. Materials Science and Engineering A, 2002, 323(1–2): 110–118

[80] Tokita M. Development of large size ceramic/metal bulls FGM fabricated by spark plasma sintering. Materials Science and Engineering, 2002, B90: 34–37

[81] Wang R, Xie Z M, Wang Y K, et al. Fabrication and characterization of nanocrystalline ODS-W via a dissolution precipitation process. International Journal of Refractory Metals & Hard Materials, 2019, 80: 104–113

[82] Wei Q, Zhang H T, Schuster B E, et al. Microstructure and mechanical properties of super-strong nanocrystalline tungsten processed by high-pressure torsion. Acta Materialia, 2006, 54: 4079–4089

[83] Guo H Y, Xia M, Chan L C, et al. Nanostructured laminar tungsten alloy with improved ductility by surface mechanical attrition treatment. Scientific Reports, 2017, 7: 1351

[84] Ma J F, Hu L Q, Liu X G, et al. Thermal stability of nanocrystallized surface layer in Al–Zn–Mg alloy by surface mechanical attrition treatment. Materials Science Forum, 2007, 546–549: 1129–1134

[85] Chang H W, Kelly P, Shi Y N, et al. Thermal stability of nanocrystallized surface produced by surface mechanical attrition treatment in aluminum alloys. Surface and Coatings Technology, 2012, 206: 3970–3980

[86] Li Y F, Chen C, Ranabhat J, et al. Formation mechanism and mechanical properties of surface nanocrystallized Ti–6Al–4V alloy processed by surface mechanical attrition treatment. Rare Metals, 2017, doi:10.1007/s12598-017-0988-4

[87] Qin W, Ren F, Doerner R P, et al. Nanochannel structures in W enhance radiation tolerance. Acta Materialia, 2018, 153: 147–155

[88] El-Atwani O, Esquivel E, Aydogan E, et al. Unprecedented irradiation resistance of nanocrystalline tungsten with equiaxed nanocrystalline grains to dislocation loop accumulation. Acta Materialia, 2019, 165: 118–128

[89] Mao H, Zhang Y, Wang J, et al. Microstructure, mechanical properties, and reinforcement mechanism of second-phase reinforced TiC-based composites: a review. Coatings, 2022, 12(6): 801

[90] Cui K, Mao H, Zhang Y, et al. Microstructure, mechanical properties, and reinforcement mechanism of carbide toughened ZrC-based ultra-high temperature ceramics: a review. Composite Interfaces, 2022, 29(7): 729–748

[91] Hammond K D, Naeger I V, Widanagamaachchi W, et al. Helium flux effects on bubble growth and surface morphology in plasma-facing tungsten from large-scale molecular dynamics simulations. Nuclear Fusion, 2019, 59: 066035

[92] Liu S G, Dai S Y, Sang C F, et al. Molecular dynamics simulation of the formation, growth and bursting of bubbles in tungsten exposed to high fluxes of low energy deuterium. Journal of Nuclear Materials, 2015, 463: 363–366

[93] Panizo-Laiz G, Díaz-Rodríguez P, Rivera A, et al. Experimental and computational studies of the influence of grain boundaries and temperature on the radiation-induced damage and hydrogen behavior in tungsten. Nuclear Fusion, 2019, 59: 086055

[94] Fu B Q, Wang J, Qiu M J, et al. Retention/reflection of hydrogen and surface evolution during cumulative bombardment of low-energy hydrogen on tungsten: a molecular dynamics study. Methods in Physics Research Section B: Beam Interactions with Materials and Atoms, 2020, 462: 55–61

[95] Piaggi P M, Bringa E M, Pasianot R C, et al. Hydrogen diffusion and trapping in nanocrystalline tungsten. Journal of Nuclear Materials, 2015, 458: 233–239

[96] Henriksson K O E, Vörtler K, Dreißigacker S, et al. Sticking of atomic hydrogen on the tungsten (0 0 1) surface. Surface Science, 2006, 600: 3167

[97] Valles G, Panizo-Laiz M, González C, et al. Influence of grain boundaries on the radiation-induced defects and hydrogen in nanostructured and coarse grained tungsten. Acta Materialia, 2017, 122: 277–286

[98] Yang X, Hassanein A. Molecular dynamics simulation of deuterium trapping and bubble formation in tungsten. Journal of Nuclear Materials, 2013, 434(1–3): 1–6

[99] Yan J, Li X, Zhu K. Fluence dependence of surface morphology and deuterium retention in W bulks and nanocrystalline W films exposed to deuterium plasma. Applied Sciences, 2021, 11: 1619

[100] El-Atwani O, Esquivel E, Efe M, et al. Loop and void damage during heavy ion irradiation on nanocrystalline and coarse grained tungsten: microstructure, effect of dpa rate, temperature, and grain size. Acta Materialia, 2018, 149: 206–219

[101] El-Atwani O, Hattar K, Hinks J A, et al. Helium bubble formation in ultrafine and nanocrystalline tungsten under different extreme conditions. Journal of Nuclear Materials, 2015, 458: 216–223

[102] Jenkins M. Characterisation of radiation-damage microstructures by TEM. Journal of Nuclear Materials, 1994, 216: 124–156

[103] Jenkins M L, Kirk M A. Characterisation of Radiation Damage by Transmission Electron Microscopy. Boca Raton, USA: CRC Press, 2000

[104] Yi X, Jenkins M L, Hattar K, et al. Characterisation of radiation damage in W and W-based alloys from 2 MeV self-ion near-bulk implantations. Acta Materialia, 2015, 92: 163–177

[105] Yabuuchi K, Saito M, Kasada R, et al. Neutron irradiation hardening and microstructure changes in Fe–Mn binary alloys. Journal of Nuclear Materials, 2011, 414(3): 498–502